Bias in mean velocities and noise in variances and covariances measured using a multistatic acoustic profiler: The Nortek Vectrino Profiler

Bias in mean velocities and noise in variances and covariances measured using a multistatic acoustic profiler: The Nortek Vectrino Profiler

Thomas R E[1,*], Schindfessel L[2,*], McLelland S J[3], Creëlle S[2], De Mulder T[2]

1 School of Earth & Environment, University of Leeds, Leeds, LS2 9JT, UK. Tel: +44 113 3436765; Fax: +44 113 3435259; E: r.e.thomas02@members.leeds.ac.uk

2 Department of Civil Engineering, Ghent University, Sint-Pietersnieuwstraat 41, 9000 Gent, Belgium. Tel: +32 9 264 32 80; Fax: +32 9 264 35 95; E: Laurent.Schindfessel@UGent.be; Stephan.Creelle@UGent.be; TomFO.DeMulder@UGent.be

3 Geography, School of Environmental Sciences, University of Hull, Hull, HU6 7RX, UK. Tel: +44 1482 465007; Fax: +44 1482 466340; E: s.j.mclelland@hull.ac.uk

* both authors contributed equally to this publication

Abstract

This paper compiles the technical characteristics and operating principles of the Nortek Vectrino Profiler and reviews previously reported user experiences. A series of experiments are then presented that investigate instrument behaviour and performance, with a particular focus on variations within the profile. First, controlled tests investigate the sensitivity of acoustic amplitude (and Signal-to-Noise Ratio, SNR) and pulse-to-pulse correlation coefficient, R^2, to seeding concentration and cell geometry. Second, a novel methodology that systematically shifts profiling cells through a single absolute vertical position investigates the sensitivity of mean velocities, SNR and noise to: (a) emitted sound intensity and the presence (or absence) of acoustic seeding; and (b) varying flow rates under ideal acoustic seeding conditions. A new solution is derived to quantify the noise affecting the two perpendicular tristatic systems of the Vectrino Profiler and its contribution to components of the Reynolds stress tensor. Results suggest that for the Vectrino Profiler:

1. optimum acoustic seeding concentrations are ~3,000 to 6,000 mg L^{-1};
2. mean velocity magnitudes are biased by variable amounts in proximal cells but are consistently underestimated in distal cells;
3. noise varies parabolically with a minimum around the “sweet spot”, 50 mm below the transceiver;

4. the receiver beams only intersect at the sweet spot and diverge nearer to and further from the transceiver. This divergence significantly reduces the size of the sampled area away from the sweet spot, reducing data quality;
5. the most reliable velocity data will normally be collected in the region between approximately 43 and 61 mm below the transceiver.

Key words: acoustic Doppler velocimetry, Vectrino Profiler, noise, bias, sensitivity

1 Introduction

Acoustic Doppler Velocimeters (ADVs) are a popular class of instrument for measuring the velocity of water. The popularity of ADVs can be attributed to their relatively low cost, portability and robustness, together with the capability to measure instantaneous at-a-point three-component velocities at sampling rates sufficient to capture turbulent flow processes in laboratory and field environments (e.g. Kraus *et al* 1994, Lohrmann *et al* 1995, Voulgaris and Trowbridge 1998, McLelland and Nicholas 2000, Garcia *et al* 2005, Chanson *et al* 2008). Recently, profiling ADVs have been developed, permitting the concurrent measurement of velocities at a number of different points (i.e. over a profile) (Lhermitte and Lemmin 1994, Lemmin and Rolland 1997, Hurther and Lemmin 1998, Zedel and Hay 2002, Craig *et al* 2011). Profiling ADVs have the obvious advantage of permitting more rapid data collection and the computation of instantaneous velocity gradients (Lhermitte and Lemmin 1994). To date, the only commercially-available profiling ADV is the Nortek Vectrino Profiler, launched in 2010.

Although the Vectrino Profiler has proved to be very popular in the scientific community, some scientists have already critiqued the quality of measurements performed with it. In work that was supported by Nortek through the provision of a Vectrino Profiler, Zedel and Hay (2011) found that neighbouring profiles of Reynolds shear stress did not overlap and that profiles of normal stresses exhibited structure that was not observed in measurements using a non-profiling ADV nor with Laser Doppler Velocimetry. In addition, they unexpectedly found non-zero mean lateral velocities, which also did not overlap between neighbouring profiles. Zedel and Hay (2011) suggested that calibration problems were the cause of these unexpected observations. Ursic *et al* (2012) towed a Vectrino Profiler at four different velocities (0.238, 0.476, 0.713 and 0.951 m s^{-1}) and at four different orientations (0, 90, 180 and 270° to the tow direction) within a 30.48 m long × 1.22 m wide × 0.61 m deep flume. They reported that the vertical extent of acceptable turbulence statistics may reduce as mean velocity

is increased, possibly due to probe head wake effects. In comparison to a non-profiling ADV, they also reported increased sensitivity of results to destructive interference associated with acoustic reflections from the bed. MacVicar *et al* (2014) critically assessed the Vectrino Profiler, focussing on apparent errors in profiles of standard deviation: the standard deviation was minimal in the "sweet spot" and increased when moving away from the sweet spot. The Signal-to-Noise Ratio (SNR) was found to affect both the mean velocity and the standard deviation of the measured velocity time series. In addition, MacVicar *et al* (2014: 1955) noted that successive profiles of mean velocity were "slightly discontinuous, but broadly consistent". The findings of Ursic *et al* (2012) and MacVicar *et al* (2014) were recently echoed by Leng and Chanson (2017) for both steady and unsteady flows. Furthermore, the knowledge center section of Nortek's website (http://www.nortek-as.com/en/knowledge-center/forum/vectrinoii) is replete with users who have observed that individual profiles of mean velocities, variances and thence turbulent kinetic energy exhibit unexpected forms and that neighbouring profiles do not overlap. Brand *et al* (2016) observed a parabolic noise profile that contaminates the variances. They attributed this to Doppler noise and showed that the noise affecting the two orthogonal systems of receivers is not equal. Consequently, the assumptions of the noise correction method of Hurther and Lemmin (2001) are not valid for the Vectrino Profiler.

Given the preceding discussion, this paper makes five contributions to the literature. First, it details the technical characteristics and operation of the Vectrino Profiler, including phase Doppler theory, the physical behaviour that yields phase shifts, the pulse-pair algorithm, ping interval and ping interval algorithm selection, the technical implementation of profiling within the Vectrino Profiler and the transformation of on-axis beam velocities to Cartesian velocities using the calibration matrix that is unique to each cell and each probe. Second, it explores the sensitivity of acoustic amplitude returns (and Signal-to-Noise Ratio, SNR) and pulse-to-pulse correlation coefficient, R^2, to seeding concentration, cell size and cell position relative to the transceiver. Third, it derives a new solution for quantifying the noise affecting the two perpendicular tristatic systems of the Vectrino Profiler and then quantifies the contribution of noise to the second order flow statistics (variances and covariances). Fourth, it quantifies the sensitivity of mean velocities, SNR and noise to emitted sound intensity (referred to as power level in Nortek's MIDAS software), acoustic seeding and flow rate. Finally, it describes and explores the cause of apparent bias in mean velocities and second order flow statistics. In making these contributions, this paper provides critical reflections on the operational principles of the Vectrino Profiler and the quality of data collected with it.

2 Vectrino Profiler: Technical characteristics and operation

The Vectrino Profiler uses similar mechanical components to the Nortek Vectrino ADV (pressure housing, acoustic transducers and probe), but it uses completely new software (Multi-Instrument Data Acquisition System; MIDAS), electronics and firmware (Craig *et al* 2011). Like the Vectrino, the Vectrino Profiler consists of a single central transceiver in conjunction with four passive receivers angled at 30° towards the transceiver. The geometrical arrangement of these components produces a focused intersection point approximately 50 mm below the transceiver (this point is known as the "sweet spot"). The transceiver emits paired acoustic pulses Δt (called the ping interval) apart that are reflected by *in situ* scattering particles or microbubbles in the water and then detected by two or more receivers (figure 1(a)). The velocity of any scatterers is estimated using the measured phase shift $\Delta\phi$ between the transmitted and received signals. Thus, a key assumption is that any acoustic scatterers are transported at the same velocity as the host fluid and that the velocity of the scatterers is a good approximation of the velocity of the host fluid. All these characteristics are the same as those of the Vectrino. However, in contrast to SonTek's LabADV and MicroADV and Nortek's NDV (e.g., Kraus *et al* 1994, Lohrmann *et al* 1995, SonTek 1997, 2001, Voulgaris and Trowbridge 1998, McLelland and Nicholas 2000), the receivers of the Vectrino Profiler work simultaneously, rather than sequentially, enabling a significant increase in the velocity sampling rate. In addition, unlike the LabADV, MicroADV and NDV, a dwell time between pulses is only necessary when using transmit pulses longer than 1 mm combined with $\Delta t < 175$ μs and is employed to avoid overheating of the acoustic transceiver. Of course, the key difference between the Vectrino Profiler and its predecessors is the ability to quasi-simultaneously sample three-component velocities at multiple locations beneath the transceiver, i.e. to collect quasi-instantaneous velocity profiles.

2.1 The pulse pair algorithm for determining the phase shift

The phase shift $\Delta\phi$ is calculated using the established pulse pair processing algorithm (Miller and Rochwarger 1972, Zrnic 1977, Lhermitte and Serafin 1984). If the complex-valued sample of pulse 1 is denoted as z_1 and the complex-valued sample of pulse 2 is denoted as z_2, the argument of their covariance is an estimate of the phase shift $\Delta\phi$ between the two pulses:

$$\Delta\phi = \arg(z_1 \cdot z_2^*) = \tan^{-1}\left[\frac{Re(z_2)Im(z_1) - Re(z_1)Im(z_2)}{Re(z_1)Re(z_2) + Im(z_1)Im(z_2)}\right] \quad (1)$$

where the asterisk denotes the complex conjugate. However, the noise associated with this estimate is substantial and must be reduced by averaging multiple pulse pairs. Denoting the actual number of pulse pairs as *NPP* and the pairs themselves as ($z_{p,1}$, $z_{p,2}$), with $NPP \geq p \geq 1$, the best estimate of the phase difference is given by (Miller and Rochwarger 1972, Zrnic 1977, Lhermitte and Serafin 1984):

$$\Delta\phi = \arg\left(\frac{1}{NPP}\sum_{p=1}^{NPP} z_{p,1} \cdot z_{p,2}^{*} \right) = \tan^{-1}\left[\frac{\sum_{p=1}^{NPP} Re(z_{p,2})Im(z_{p,1}) - Re(z_{p,1})Im(z_{p,2})}{\sum_{p=1}^{NPP} Re(z_{p,1})Re(z_{p,2}) + Im(z_{p,1})Im(z_{p,2})}\right] \quad (2)$$

Additionally, when multiple pairs are averaged, it is possible to define a complex-valued correlation coefficient R^2 by normalizing the correlation of the signals with their energy (Zedel *et al* 1996, Zedel 2008):

$$R^2 = \frac{\sum_{p=1}^{NPP} z_{p,1} \cdot z_{p,2}^{*}}{\sum_{p=1}^{NPP} |z_{p,1}| \cdot |z_{p,2}|} \quad (3)$$

Note that the phase shift $\Delta\phi$ can be calculated directly from R^2, since $\Delta\phi = \arg(R^2)$. The modulus operators in the denominator are approximated using the "alpha-max plus beta-min" algorithm, which introduces a periodicity of $\pi/4$ rad with maxima at $\pm k\pi/4$ rad (k even), minima at $\pm l\pi/8$ rad (l odd) and a potential error of up to ~4% in R^2-values, but this should have no influence on velocity estimates (R. Craig, personal communication, 4 September, 2012). Following Zedel (2008), equation (3) can be rewritten as:

$$R^2 = \frac{\sum_{p=1}^{NPP} z_{p,1} \cdot (z_{p,1} e^{-i\Delta\phi} + N e^{-i\gamma})}{\sum_{p=1}^{NPP} |z_{p,1}| \cdot |z_{p,1} e^{-i\Delta\phi} + N e^{-i\gamma}|} \quad (4)$$

where $z_{p,2}$ has been expressed as $z_{p,1}e^{-i\Delta\phi} + Ne^{-i\gamma}$ to explicitly show that $z_{p,2}$ comprises a term due to the phase-shifted emitted pulse, $z_{p,1}e^{-i\Delta\phi}$, and a term due to incoherent backscatter (noise) caused by random fluid motions and changes in backscatter strength, $Ne^{-i\gamma}$, where N is the amplitude of the incoherent backscatter and γ is a random angle. The magnitude of R^2 is therefore a measure of the energy in coherent backscatter relative to the total backscatter energy (Zedel 2008) or of the consistency of the phase shift of each sample, and can be used to assess data quality. If N is small, $R^2 \rightarrow 1$ and estimates of $\Delta\phi$ are reliable. Conversely, if N is large,

R^2 decreases and estimates of $\Delta\phi$ are less reliable since the phase difference between $z_{p,1}$ and N is random (Zedel 2008). Low R^2-values indicate unreliable estimates of phase because they signify the violation of assumptions about the width and shape of the signal spectral density function used to estimate the phase of the received signal (Lhermitte and Serafin 1984). For non-profiling ADVs, the acceptable lower bound for R^2 is 70% (Nortek 1997), but it is unclear whether this bound applies to the Vectrino Profiler.

2.2 Calculating fluid velocity from phase shift

For the case of a single pulse-pair and a bistatic system with one transceiver and one receiver depicted in figure 1(b), the time rate of change of the distances between a scatterer and the transceiver, ΔR_T, and a scatterer and a receiver, ΔR_R, are (Zedel 2008, Kalantari *et al* 2009):

$$\frac{\Delta R_T}{\Delta t} = V\cos(\delta + \beta/2) \quad (5)$$

$$\frac{\Delta R_R}{\Delta t} = V\cos(\delta - \beta/2) \quad (6)$$

where the velocity, V, makes a random angle δ with the bisector of the angle β between the paths of the transmitted and received pulses. The time rate of change of total travel distance of a pulse ($\Delta R = \Delta R_T + \Delta R_R$) is thus:

$$\frac{\Delta R}{\Delta t} = V\left[\cos\left(\delta + \frac{\beta}{2}\right) + \cos\left(\delta - \frac{\beta}{2}\right)\right] = 2V\cos(\delta)\cos\left(\frac{\beta}{2}\right) = 2V_b\cos\left(\frac{\beta}{2}\right) \quad (7)$$

where the velocity $V_b = V\cos(\delta)$ is introduced, denoting the velocity projected onto the bisector (figure 1(b)). This velocity is called the beam velocity, and is the rawest velocity estimate that the user can obtain from the Vectrino Profiler.

Next, the phase shift $\Delta\phi$ between the two pulses is expressed as:

$$\Delta\phi = \frac{2\pi f}{c}\Delta R = \frac{2\pi f}{c}2V_b\cos\left(\frac{\beta}{2}\right)\Delta t \quad (8)$$

where f is the frequency of sound emitted by the transceiver (10 MHz in the case of the Vectrino

Profiler), and c is the speed of sound within the fluid (≈1480 m s^{-1}, dependent on temperature and salinity). Rearranging, V_b can be written as a function of the measured phase shift:

$$V_b = \frac{c}{4\pi f}\frac{1}{\cos\left(\frac{\beta}{2}\right)}\frac{\Delta\phi}{\Delta t} \quad (9)$$

Note that the effect of the Doppler shift on the frequency is neglected, which is a good approximation given the magnitude of the speed of sound compared to the measured velocity. Although equation (9) was derived for a single pulse-pair, the same equation is adopted when multiple pulse-pairs are averaged to determine a more robust estimate of $\Delta\phi$.

2.3 Velocity ambiguity and the dual pulse-pair repetition scheme

The phase angle from which the velocity is determined can only be resolved within the range $-\pi$ to $+\pi$ due to the periodicity of the arctangent function in equation (2); if $\Delta\phi$ falls outside this range, phase wrapping or aliasing will occur (Franca and Lemmin 2006). This is termed the ambiguity problem on the phase shift and is associated with a similar ambiguity on the velocity. By substituting the maximum phase shift ($\Delta\phi = \pi$) that can be resolved unambiguously into equation (9), the ambiguity velocity V_{bmax} is found to be $c/[4f\Delta t\cos(\beta/2)]$. However, by convention, the ambiguity velocity is given by $c/(4f\Delta t)$ and therefore the $1/\cos(\beta/2)$ factor is incorporated within the calibration matrix that is used to transform beam velocities to three-component Cartesian velocities (see equation (13C)). For single pulse-pairs, the phase shift can be kept within the $[-\pi, +\pi]$ interval by increasing Δt, which in practice is achieved by increasing the velocity range specified in MIDAS. Wrapping or aliasing can be identified as a sudden jump in velocity, typically with a change of sign (Franca and Lemmin 2006, Hurther *et al* 2011). Although aliasing should be avoided whenever possible, aliased data may be corrected during post-processing by applying unwrappers to raw phase shifts recovered from beam velocities. 1-D unwrappers (e.g., Franca and Lemmin 2006, Hurther *et al* 2011) may be applied to phase time-series collected by a single beam in a single cell, 2-D unwrappers may be applied to phase time-series collected by a single beam in more than one cell, or 3-D unwrappers may be applied to phase time-series collected by more than one beam in more than one cell and arranged into a 3-D array (e.g., Ghiglia and Pritt 1998, Zappa and Busca 2008, Parkhurst *et al* 2011).

To measure velocities faster than V_{bmax}, a dual pulse-pair repetition scheme is implemented in the Vectrino Profiler. This scheme uses two pulse-pairs with unequal spacing in time, Δt_1 and Δt_2. To obtain a single velocity measurement with the dual pulse-pair scheme, the central transceiver emits three acoustic pulses Δt_1 and Δt_2 apart, where $\Delta t_1 < \Delta t_2$, which yield two separate estimates of phase shift, $\Delta\phi_1$ and $\Delta\phi_2$, that are used to estimate the beam velocity:

$$V_b = \frac{c}{4\pi f}\frac{1}{\cos\left(\frac{\beta}{2}\right)}\frac{(\Delta\phi_2-\Delta\phi_1)}{(\Delta t_2-\Delta t_1)} \quad (10)$$

Using unequal pulse-pairs extends the velocity range since the ambiguity velocity is then defined by the difference between the pulse-pair intervals: $c/(4f[\Delta t_2 - \Delta t_1])$. However, signal noise limits the usable time difference (Craig *et al* 2011).

Again, multiple sets of dual pulses are averaged to obtain a more reliable estimate of $\Delta\phi$. For a given sampling frequency (f_s), the number of pulse-pairs averaged by the Vectrino Profiler is given by:

$$NPP = \begin{cases} \left\lfloor \frac{f_s}{\Delta t+\Delta t_D} - 2 \right\rfloor & \text{For single pulse pairs} \\ \left\lfloor \frac{f_s}{(\Delta t_1+\Delta t_2+\Delta t_D)} - 2 \right\rfloor & \text{For dual pulse pairs} \end{cases} \quad (11)$$

where Δt_D is the dwell time introduced when transmit pulses longer than 1 mm are combined with Δt < 175 μs, and is normally ~185 μs per measurement cycle. The ping interval Δt can vary between ~1300 μs and ~108 μs, with the upper limit being influenced by turbulence decorrelation and the lower limit being the shortest time between pulses to prevent echoes from adjacent pulses interfering with each other. Note that unlike the Nortek NDV (Nortek 1997), no additional computational processing time is required during each measurement cycle. In addition, when unequal pulse-pairs are used to measure faster velocities there is a decrease in *NPP* since each velocity calculation requires a separate dual pulse-pair.

2.4 Ping interval algorithms

In MIDAS, three algorithms are available to set the appropriate ping interval, Δt:

A. The maximum interval algorithm selects Δt to achieve the desired ambiguity velocity. If $2\Delta R_T / c > \Delta t$ where ΔR_T is the vertical distance from the transceiver to the centroid of the farthest sampled "cell", the dual pulse-pair repetition scheme is used to set Δt_1 and Δt_2. Maximizing Δt is beneficial for data quality, because a larger Δt results in a larger phase difference for a given beam velocity (equations (9) and (10)), increasing the resolution of beam velocity estimates. In the authors' experience, provided that the flow is well seeded (i.e., correlations > 90%, SNRs > 30 dB) and the user has a good *a priori* estimate of the largest velocity magnitude, the maximum interval algorithm results in the highest data quality.

B. The minimum interval algorithm estimates Δt as $2\Delta R_T / c$, which produces the smallest possible Δt needed to sample within the farthest sampled "cell" and generally results in an ambiguity velocity which is much larger than that entered by the user. Reduced Δt yields a smaller phase difference for a given beam velocity (equations (9) and (10)), reducing the resolution of beam velocity estimates. Conversely, by minimizing Δt, the minimum interval algorithm results in a larger number of pulse pairs being averaged together, which reduces electrical noise. Nortek (2015a) suggest that the minimum interval algorithm might be a preferable choice in highly turbulent flow.

C. The adaptive interval algorithm examines profiles of acoustic backscatter from all four receivers and estimates the temporal position of acoustic interference in the backscatter. It then selects Δt to achieve the desired ambiguity velocity and maximum sampling range while minimising/removing acoustic interference. If the environment is likely to change significantly during data collection, the user may request the ping interval to be adjusted dynamically throughout data collection. Despite advice within Nortek's Software User Guide (Nortek 2015a) that the adaptive interval algorithm "is the best general choice", in the authors' experience, it switches too readily between rather high and rather low ambiguity velocities, so that although it may minimise acoustic interference, it results in aliasing and poor data quality.

2.5 The technical implementation of profiling and its consequences

For a non-profiling ADV such as the Vector or Vectrino, a combination of the probe geometry (a bistatic angle, $\beta/2$, of 15°) and the known travel time of the emitted acoustic pulse ensures that the signal is sampled at the sweet spot, where the received signal is at its strongest (McLelland and Nicholas 2000). This part of the signal is then sampled and processed to

estimate the time rate of change of phase, $\Delta\phi/\Delta t$, using the pulse-pair algorithm (section 3.1, Miller and Rochwarger 1972, Zrnic 1977, Lhermitte and Serafin 1984). For a non-profiling ADV, the structure of the received signal has been thoroughly explained by McLelland and Nicholas (2000, their figure 2). For the Vectrino Profiler, instead of sampling the received signal at a single instant in time following pulse emission, the signal is range gated such that it is sampled at multiple time delays corresponding to the travel time from the centroid of each sampled "cell" (figure 2). The different samples are then processed separately to estimate the phase shift $\Delta\phi$ in each cell and thence the velocity (Lemmin and Roland 1997). After an initial peak due to the emission of the acoustic pulse (transmit noise; not shown), the signal strength peaks when the reflection from the sampling volume reaches the receivers and then drops asymptotically to a background level, corresponding to the (electronic) system noise (figure 2). The received signal is not a step function, but instead varies smoothly because of noise and the high number of scatterers within the sampling volume (figure 2). Range gating enables beam velocity measurements to be measured between 20 and 96 mm below the central transceiver, with a transformation to orthogonal velocity components calibrated for a region between 40 and 74 mm below the transceiver (Craig *et al* 2011). The bistatic angle, $\beta/2$, therefore varies within the calibrated region, with the ideal value (15°) only occurring at the sweet spot (~50 mm below the transceiver).

A combination of the smoothly varying nature of the received signal and these geometric considerations cause vertical profiles of the signal-to-noise ratio, SNR, to be parabolic, with the peak signal strength and highest SNR occurring at the sweet spot. Concurrently, other cells have reduced SNR. SNR (in dB) is the difference between the signal strength (in dB) and background noise (in dB):

$$\text{SNR} = \text{signal amplitude} - \text{noise amplitude} \quad (12)$$

where the noise amplitude is determined at the start of a measurement by activating the receivers without activating the transceiver (Nortek 2012). This approach adequately quantifies background noise if that noise is temporally invariant but it is incapable of accounting for temporal variations and, crucially, the effects of constructive and destructive interference are included within the signal rather than the noise. Thus, measurements that suffer from interference may exhibit erroneously large SNR-values, and SNR is not a reliable metric for assessing data quality in these circumstances.

Nortek state that SNR should be at least 20 dB in distal and proximal cells and at least 30 dB in the sweet spot (Nortek 2013, MacVicar *et al* 2014). SNR may be improved by increasing the power of the emitted pulse or increasing the number of scatterers in the sampling volume. The latter may be achieved by either adding seeding particles or increasing the transmit pulse size, which is the length of the transmitted acoustic pulse in conjunction with individual cell size. Since the sampling volume of an individual cell is $\pi(d_1^2+d_2^2)L/8$, where d_1 and d_2 are the diameters of the transmitted beam at the top and bottom of a cell and L is the cell size (= cell height), the number of scatterers in the sampling volume increases at least linearly with cell size (depending on the beam spread). Within MIDAS, the user may select the cell size to be 1, 2, 3 or 4 mm; changing the cell size automatically changes the transmit pulse size to match (Nortek 2015a). Increasing cell size and transmit pulse size thus increases the number of scatterers contributing to sampled echo and the phase estimate at a specific instant in time.

2.6 Transformation of beam velocities to three-component velocities

Equations (9) and (10) presented how the beam velocity is calculated for a system of one transceiver and one receiver. Since the Vectrino Profiler consists of four receivers operating simultaneously, four beam velocities are measured, each one being a projection of the true velocity vector onto the corresponding bisector (figure 1(b)). The on-axis beam velocities may be transformed to a Cartesian reference frame. Conventionally, the streamwise velocity, u, is perpendicular to the probe axis and points in the direction of the first receiver (marked with a red collar, figure 3(a)), the vertical velocity, w, points towards the transceiver, and the cross-stream velocity, v, is perpendicular to both u and w, as defined by the right-handed coordinate system and points towards the second receiver. For a perfectly manufactured device, receivers 1 and 3 are coplanar and orthogonal to receivers 2 and 4. Therefore, the first two measure u and w_1, while the latter two measure v and w_2, where w_1 and w_2 are independent measurements of the vertical velocity. The transformation from beam velocities V_{b1}, V_{b2}, V_{b3} and V_{b4} to Cartesian velocities u, v, w_1 and w_2 is found through multiplication by an appropriate matrix:

$$\begin{bmatrix} u_i \\ v_i \\ w_{1,i} \\ w_{2,i} \end{bmatrix} = \mathbf{T}_i \begin{bmatrix} V_{b1,i} \\ V_{b2,i} \\ V_{b3,i} \\ V_{b4,i} \end{bmatrix} \quad (13A)$$

where:

$$\mathbf{T}_i = \begin{bmatrix} a_{11,i} & a_{12,i} & a_{13,i} & a_{14,i} \\ a_{21,i} & a_{22,i} & a_{23,i} & a_{24,i} \\ a_{31,i} & a_{32,i} & a_{33,i} & a_{34,i} \\ a_{41,i} & a_{42,i} & a_{43,i} & a_{44,i} \end{bmatrix} \quad (13B)$$

For a perfectly manufactured device,

$$\mathbf{T}_i = \begin{bmatrix} \frac{\cos(\beta_i/2)}{\sin\beta_i} & 0 & \frac{-\cos(\beta_i/2)}{\sin\beta_i} & 0 \\ 0 & \frac{\cos(\beta_i/2)}{\sin\beta_i} & 0 & \frac{-\cos(\beta_i/2)}{\sin\beta_i} \\ \frac{\cos(\beta_i/2)}{(1+\cos\beta_i)} & 0 & \frac{\cos(\beta_i/2)}{(1+\cos\beta_i)} & 0 \\ 0 & \frac{\cos(\beta_i/2)}{(1+\cos\beta_i)} & 0 & \frac{\cos(\beta_i/2)}{(1+\cos\beta_i)} \end{bmatrix} \quad (13C)$$

Note that the cell number *i* is introduced for the first time here, denoting the i^{th} velocity profiling cell away from the transceiver. As cell location determines the angle β_i, each cell has a unique transformation matrix $\mathbf{T}_i$. Note also that equation (13C) has been written to explicitly show the $\cos(\beta_i/2)$ factor from the ambiguity velocity equation and can be simplified through use of the double angle formulae. Due to production tolerances, in practice $\mathbf{T}_i$ differs somewhat from the ideal values presented in equation (13C) and is obtained through calibration. This calibration is stored within the firmware of each probe in fixed point integer form (R. Craig, personal communication, 18th August, 2014), and is part of the MATLAB .mat file exported by MIDAS. When cell sizes larger than 1 mm are used, MIDAS averages the calibration matrices for the 1 mm cells that constitute the larger cells and then truncates the resulting matrix to fixed point integer form (R. Craig, personal communication, 18th August, 2014).

3 Experimental Methodology

To investigate the behaviour and to assess the performance of the Vectrino Profiler, three separate experiments were performed. First, systematic tests (Experiment 1) were undertaken using a beaker emplaced on a magnetic stirrer to assess the sensitivity of amplitude and correlation to the concentration of acoustic seeding. Second, a flume experiment (Experiment 2) was undertaken to assess the internal consistency of velocities and noise in neighbouring

cells in a single profile at a range of transceiver power settings and seeding concentrations. Third, a flume experiment (Experiment 3) was undertaken to assess the internal consistency of velocities and noise in neighbouring cells in a single profile at two different flow rates under optimal seeding conditions. All experiments were undertaken with Vectrino Profilers purchased prior to the introduction of modified receiver ceramics and a modified calibration procedure in May 2016. The following sections present the methodologies of all three experiments.

3.1 Experiment 1: Sensitivity of amplitude and correlation to the concentration of acoustic seeding

Tests were undertaken in which the concentration of the acoustic seeding material Talisman 10 (specific gravity 0.99), pre-sieved to retain only the portion of the particle size distribution between 20 and 100 μm, was systematically increased in a 6 L beaker that was initially filled with distilled water. A magnetic stirrer was used to maintain the seeding material in suspension. The Vectrino Profiler with probe and hardware serial numbers VCN8374 and VNO1256, respectively, was mounted 200 mm above the bottom of the beaker; the profiling region was thus 126-160 mm above the bottom of the beaker, sufficiently far away to avoid interaction with the stirrer. The vertical location of the probe head was set using the bottom check facility afforded by the Vectrino Profiler (±0.1 mm) and verified using a steel rule (±0.5 mm). Velocities, amplitudes and correlations were monitored at 100 Hz for 240 s, yielding 24,000 samples in each cell. The firmware and software was version 1.20.1698, dating from December 2012. The ping interval algorithm was set to maximum interval and the velocity range was set to 0.4 m s^{-1}, equivalent to a beam ambiguity velocity of 0.113 m s^{-1}.

3.2 Experiment 2: Internal consistency of velocities and noise in neighbouring cells in a single profile at a range of transceiver power settings and seeding concentrations

Velocity profiles were sampled at a series of overlapping vertical positions in a 2.6 m long × 0.082 m wide × 0.120 m deep Plexiglas recirculating flume at Ghent University, Belgium. The flume slope was set to 0 m m^{-1}, water depth at the measurement location was 0.114 m and the discharge was 0.00116 m^3s^{-1}. Velocities were first sampled in 'clear' tap water (with no added acoustic seeding material) and tests were undertaken using three different power settings ('low', 'high−', and 'high'). Referenced to 1 μPa at 1 m, these settings correspond to emitted sound intensity levels of 150 dB, 162 dB, and 168 dB, respectively (Poindexter *et al* 2011).

During a second series of experiments, power was set to 'high' and kaolin (D_{15} = 0.8 µm, D_{85} = 1 µm) was suspended in the water until the flow was saturated and SNR remained constant. This condition corresponded to the maximum SNR that could be achieved without continuous feeding of seeding material. Measurements were then repeated with the Vectrino Profiler in the same orientation and also rotated by 90° and 180° relative to the flume axis.

In both test series, the Vectrino Profiler with probe and hardware serial numbers VCN8472 and VNO1322, respectively, was mounted on a thumb screw with a measurement accuracy of 0.1 mm and set to sample velocities in 16, 2 mm high, cells at 30 Hz for 120 seconds at a height of 60 mm above the flume floor. The probe was then moved downwards by 2 mm, corresponding to the height of one cell. As a consequence, the point that was located in the i^{th} cell during the first recording was now located in the $(i-1)^{th}$ cell. Iteratively, a set of 16 measurements was performed in increasingly lower positions, until the 16^{th} cell of the first recording was located in the 1^{st} cell of the last recording (figure 3(b)). This methodology yielded one vertical location (30 mm above the bottom) in which the velocity was sampled 16 times but in different cells (i.e. in different positions relative to the transceiver). If the Vectrino Profiler performed consistently over the entire profile, the 16 evaluations of mean velocities and second order statistics would be equal at this vertical location since the blockage ratio (projected immersed probe area/flume cross-sectional area) only increased from 4.44% to 6.69%.

The firmware and software was version 1.22.1950, dating from August 2013. The ping interval algorithm was set to maximum interval and the velocity range was set to 0.5 m s^{-1}, which was sufficiently high to avoid destructive interference associated with multiple reflections of the emitted sound from the bottom back to the sampling volume and also from the bottom to the water surface and back to the sampling volume (Nortek 2013). Sampled velocities were despiked using the algorithm proposed by Wahl (2003). Typically, the number of detected spikes was low: less than 2% of the collected data.

3.3 Experiment 3: Internal consistency of velocities and noise in neighbouring cells in a single profile under optimal seeding conditions

In this experiment, velocity profiles were sampled at a series of overlapping vertical positions in a 10 m long × 0.3 m wide × 0.5 m deep glass-walled Armfield™ recirculating flume at the University of Hull, UK. The flume was filled one particle deep with 2-4 mm gravel clasts that were immobile at the imposed flow rates (pump frequencies of 10 Hz and 25 Hz, generating

depth-averaged velocities of 0.118 and 0.331 m s^{-1}, respectively) and slope (0 m m^{-1}). Mean water depth was held constant across all experiments at 0.15 m and Talisman 10, pre-sieved to retain only the portion of the particle size distribution between 20 and 100 μm, was used to set seeding concentration to 3,000 mg L^{-1}. The Vectrino Profiler with probe and hardware serial numbers VCN8374 and VNO1256, respectively, was mounted on a thumb screw and set to sample velocities in 35, 1 mm high, cells at 100 Hz for 240 s. A similar methodology to experiment 2 was adopted, except that 4 mm vertical increments were used and the bottom check facility afforded by the Vectrino Profiler was used to assess those increments. Likewise, if the Vectrino Profiler performed consistently over the entire profile, the nine evaluations of mean velocities and second order statistics would be equal since the blockage ratio (projected immersed probe area/flume cross-sectional area) only increased from 1.29% to 1.85%.

The firmware and software was version 1.20.1698, dating from December 2012. The ping interval algorithm was set to maximum interval and the velocity range was set to 0.3, 1.3 or 2.4 m s^{-1} (equivalent to a beam ambiguity velocity of 0.085, 0.185 or 0.342 m s^{-1}, respectively), depending on the pump frequency. These velocity ranges were sufficiently high to avoid aliasing and any destructive interference. Sampled velocities were despiked using the algorithm proposed by Wahl (2003); the number of detected spikes was always less than 1% of the collected data.

4 Data quality assessment

4.1 Quantification and correction of noise

As noted previously, the geometry of a perfectly manufactured Vectrino Profiler yields two independent measurements of the vertical velocity, w_1 and w_2. Hurther and Lemmin (2001) and Blanckaert and Lemmin (2006) showed that the covariances, $\overline{uv}$, $\overline{uw_2}$ and $\overline{vw_1}$, and variance $\overline{w_1 w_2}$ are free of noise but the variances, $\overline{u^2}$, $\overline{v^2}$, $\overline{{w_1}^2}$, and $\overline{{w_2}^2}$ contain noise. In practice, the Vectrino Profiler is unlikely to be perfectly manufactured and these statements may not be true (Brand *et al* 2016). Following Lohrmann *et al* (1995) and Voulgaris and Trowbridge (1998), if equation (13B) is used to expand equation (13A) and it is explicitly recognised that measured beam velocities, V_b, consist of the true velocity, $\widehat{V_b}$, plus unbiased noise, n (where $\bar{n} \equiv 0$), the following equations are obtained:

$$u_i = a_{11,i}\left(\widehat{V_{b1,\iota}} + n_{1,i}\right) + a_{12,i}\left(\widehat{V_{b2,\iota}} + n_{2,i}\right) + a_{13,i}\left(\widehat{V_{b3,\iota}} + n_{3,i}\right) + a_{14,i}\left(\widehat{V_{b4,\iota}} + n_{4,i}\right) \quad (14A)$$

$$v_i = a_{21,i}\left(\widehat{V_{b1,\iota}} + n_{1,i}\right) + a_{22,i}\left(\widehat{V_{b2,\iota}} + n_{2,i}\right) + a_{23,i}\left(\widehat{V_{b3,\iota}} + n_{3,i}\right) + a_{24,i}\left(\widehat{V_{b4,\iota}} + n_{4,i}\right) \quad (14B)$$

$$w_{1,i} = a_{31,i}\left(\widehat{V_{b1,i}} + n_{1,i}\right) + a_{32,i}\left(\widehat{V_{b2,i}} + n_{2,i}\right) + a_{33,i}\left(\widehat{V_{b3,i}} + n_{3,i}\right) + a_{34,i}\left(\widehat{V_{b4,i}} + n_{4,i}\right) \quad (14C)$$

$$w_{2,i} = a_{41,i}\left(\widehat{V_{b1,i}} + n_{1,i}\right) + a_{42,i}\left(\widehat{V_{b2,i}} + n_{2,i}\right) + a_{43,i}\left(\widehat{V_{b3,i}} + n_{3,i}\right) + a_{44,i}\left(\widehat{V_{b4,i}} + n_{4,i}\right) \quad (14D)$$

In the absence of noise, the products $\overline{w_1{}^2}$, $\overline{w_1 w_2}$, and $\overline{w_2{}^2}$ are equal. To quantify noise, previous investigators (Lohrmann *et al* 1995, Voulgaris and Trowbridge 1998, Hurther and Lemmin 2001) assumed that noise is independent of the velocity fluctuations, noise fluctuations in independent receivers are uncorrelated, and all receivers are identical. If the latter assumption is relaxed by assuming that the noise of opposite beams (i.e., beams 1 and 3 and beams 2 and 4) have identical variances, equations (14C) and (14D) can be used to write:

$$\begin{aligned}\overline{w_{1,i}{}^2} = {} & a_{31,i}{}^2\left(\overline{\widehat{V_{b1,i}}^{\,2}} + \sigma_{13,i}{}^2\right) + a_{32,i}{}^2\left(\overline{\widehat{V_{b2,i}}^{\,2}} + \sigma_{24,i}{}^2\right) + a_{33,i}{}^2\left(\overline{\widehat{V_{b3,i}}^{\,2}} + \sigma_{13,i}{}^2\right) \\ & + a_{34,i}{}^2\left(\overline{\widehat{V_{b4,i}}^{\,2}} + \sigma_{24,i}{}^2\right) + 2a_{31,i}a_{32,i}\overline{\widehat{V_{b1,i}}\widehat{V_{b2,i}}} + 2a_{31,i}a_{33,i}\overline{\widehat{V_{b1,i}}\widehat{V_{b3,i}}} \\ & + 2a_{31,i}a_{34,i}\overline{\widehat{V_{b1,i}}\widehat{V_{b4,i}}} + 2a_{32,i}a_{33,i}\overline{\widehat{V_{b2,i}}\widehat{V_{b3,i}}} + 2a_{32,i}a_{34,i}\overline{\widehat{V_{b2,i}}\widehat{V_{b4,i}}} \\ & + 2a_{33,i}a_{34,i}\overline{\widehat{V_{b3,i}}\widehat{V_{b4,i}}}\end{aligned} \quad (15A)$$

$$\begin{aligned}\overline{w_{1,i}w_{2,i}} = {} & a_{31,i}a_{41,i}\left(\overline{\widehat{V_{b1,i}}^{\,2}} + \sigma_{13,i}{}^2\right) + a_{32,i}a_{42,i}\left(\overline{\widehat{V_{b2,i}}^{\,2}} + \sigma_{24,i}{}^2\right) \\ & + a_{33,i}a_{43,i}\left(\overline{\widehat{V_{b3,i}}^{\,2}} + \sigma_{13,i}{}^2\right) + a_{34,i}a_{44,i}\left(\overline{\widehat{V_{b4,i}}^{\,2}} + \sigma_{24,i}{}^2\right) \\ & + \left(a_{31,i}a_{42,i} + a_{32,i}a_{41,i}\right)\overline{\widehat{V_{b1,i}}\widehat{V_{b2,i}}} + \left(a_{31,i}a_{43,i} + a_{33,i}a_{41,i}\right)\overline{\widehat{V_{b1,i}}\widehat{V_{b3,i}}} \\ & + \left(a_{31,i}a_{44,i} + a_{34,i}a_{41,i}\right)\overline{\widehat{V_{b1,i}}\widehat{V_{b4,i}}} + \left(a_{33,i}a_{42,i} + a_{32,i}a_{43,i}\right)\overline{\widehat{V_{b2,i}}\widehat{V_{b3,i}}} \\ & + \left(a_{32,i}a_{44,i} + a_{34,i}a_{42,i}\right)\overline{\widehat{V_{b2,i}}\widehat{V_{b4,i}}} + \left(a_{33,i}a_{44,i} + a_{34,i}a_{43,i}\right)\overline{\widehat{V_{b3,i}}\widehat{V_{b4,i}}}\end{aligned} \quad (15B)$$

$$\begin{aligned}\overline{w_{2,i}{}^2} = {} & a_{41,i}{}^2\left(\overline{\widehat{V_{b1,i}}^{\,2}} + \sigma_{13,i}{}^2\right) + a_{42,i}{}^2\left(\overline{\widehat{V_{b2,i}}^{\,2}} + \sigma_{24,i}{}^2\right) + a_{43,i}{}^2\left(\overline{\widehat{V_{b3,i}}^{\,2}} + \sigma_{13,i}{}^2\right) \\ & + a_{44,i}{}^2\left(\overline{\widehat{V_{b4,i}}^{\,2}} + \sigma_{24,i}{}^2\right) + 2a_{41,i}a_{42,i}\overline{\widehat{V_{b1,i}}\widehat{V_{b2,i}}} + 2a_{41,i}a_{43,i}\overline{\widehat{V_{b1,i}}\widehat{V_{b3,i}}} \\ & + 2a_{41,i}a_{44,i}\overline{\widehat{V_{b1,i}}\widehat{V_{b4,i}}} + 2a_{42,i}a_{43,i}\overline{\widehat{V_{b2,i}}\widehat{V_{b3,i}}} + 2a_{42,i}a_{44,i}\overline{\widehat{V_{b2,i}}\widehat{V_{b4,i}}} \\ & + 2a_{43,i}a_{44,i}\overline{\widehat{V_{b3,i}}\widehat{V_{b4,i}}}\end{aligned} \quad (15C)$$

where $\sigma_{13}^2 = \overline{n_1^2} = \overline{n_3^2}$ and $\sigma_{24}^2 = \overline{n_2^2} = \overline{n_4^2}$. Equations for the other variances and covariances are provided in the Appendix. In all cases, the first four terms involve the total variance of the measured velocity and the last six terms contain cross-products between beams to which the uncorrelated Doppler noise has no contribution. The sums of the cross-multiplied calibration matrix elements $\sum_{j=1}^{j=4} a_{1j}^2$, $\sum_{j=1}^{j=4} a_{1j}a_{2j}$, $\sum_{j=1}^{j=4} a_{1j}a_{3j}$, $\sum_{j=1}^{j=4} a_{1j}a_{4j}$, $\sum_{j=1}^{j=4} a_{2j}^2$, $\sum_{j=1}^{j=4} a_{2j}a_{3j}$, $\sum_{j=1}^{j=4} a_{2j}a_{4j}$, $\sum_{j=1}^{j=4} a_{3j}^2$, $\sum_{j=1}^{j=4} a_{3j}a_{4j}$, and $\sum_{j=1}^{j=4} a_{4j}^2$, dictate how noise is propagated into variance and covariance estimates. The magnitudes of these "noise multipliers" are shown in table 1 for an example probe. It is clear that for this example probe, $\overline{uv}$ is not noise free for much of the sampled profile, but that the magnitude of the noise in $\overline{u^2}$ and $\overline{v^2}$ is 25 to 39 times that in $\overline{uv}$, and 11 to 16 times that in $\overline{w_1^2}$ and $\overline{w_2^2}$. Conversely, $\overline{w_1 w_2}$ is virtually noise free (maximum noise multiplier = 0.005).

The differences $\overline{w_1^2} - \overline{w_1 w_2}$ and $\overline{w_2^2} - \overline{w_1 w_2}$ can be used to quantify the noise associated with the two independent measurements of the variance of vertical velocity:

$$\overline{w_{1,i}^2} - \overline{w_{1,i}w_{2,i}} = \overbrace{\widehat{w_{1,i}^2} - \widehat{\overline{w_{1,i}w_{2,i}}}}^{=0} + \left[a_{31,i}\left(a_{31,i} - a_{41,i}\right) + a_{33,i}\left(a_{33,i} - a_{43,i}\right)\right]\sigma_{13,i}^2 + \left[a_{32,i}\left(a_{32,i} - a_{42,i}\right) + a_{34,i}\left(a_{34,i} - a_{44,i}\right)\right]\sigma_{24,i}^2 \quad (16A)$$

$$\overline{w_{2,i}^2} - \overline{w_{1,i}w_{2,i}} = \overbrace{\widehat{w_{2,i}^2} - \widehat{\overline{w_{1,i}w_{2,i}}}}^{=0} + \left[a_{41,i}\left(a_{41,i} - a_{31,i}\right) + a_{43,i}\left(a_{43,i} - a_{33,i}\right)\right]\sigma_{13,i}^2 + \left[a_{42,i}\left(a_{42,i} - a_{32,i}\right) + a_{44,i}\left(a_{44,i} - a_{34,i}\right)\right]\sigma_{24,i}^2 \quad (16B)$$

where the circumflexes are used to denote the noise-free terms in equations (15A) to (15C). Consideration of the magnitudes of the terms in equations (16) indicates that equation (16A) is dominated by terms associated with beams 1 and 3, and equation (16B) is dominated by terms associated with beams 2 and 4. Nevertheless, after substitution and elimination,

$$\sigma_{13,i}{}^2$$

$$= \frac{\begin{matrix}\left[a_{42,i}\left(a_{42,i}-a_{32,i}\right)+a_{44,i}\left(a_{44,i}-a_{34,i}\right)\right]\left(\overline{w_{1,\iota}{}^2}-\overline{w_{1,\iota}w_{2,\iota}}\right)\\ -\left[a_{32,i}\left(a_{32,i}-a_{42,i}\right)+a_{34,i}\left(a_{34,i}-a_{44,i}\right)\right]\left(\overline{w_{2,\iota}{}^2}-\overline{w_{1,\iota}w_{2,\iota}}\right)\end{matrix}}{\left(\begin{matrix}\left[a_{31,i}\left(a_{31,i}-a_{41,i}\right)+a_{33,i}\left(a_{33,i}-a_{43,i}\right)\right]\left[a_{42,i}\left(a_{42,i}-a_{32,i}\right)+a_{44,i}\left(a_{44,i}-a_{34,i}\right)\right]\\ -\left[a_{41,i}\left(a_{41,i}-a_{31,i}\right)+a_{43,i}\left(a_{43,i}-a_{33,i}\right)\right]\left[a_{32,i}\left(a_{32,i}-a_{42,i}\right)+a_{34,i}\left(a_{34,i}-a_{44,i}\right)\right]\end{matrix}\right)} \quad (17A)$$

$$\sigma_{24,i}{}^2$$

$$= \frac{\begin{matrix}\left[a_{31,i}\left(a_{31,i}-a_{41,i}\right)+a_{33,i}\left(a_{33,i}-a_{43,i}\right)\right]\left(\overline{w_{2,\iota}{}^2}-\overline{w_{1,\iota}w_{2,\iota}}\right)\\ -\left[a_{41,i}\left(a_{41,i}-a_{31,i}\right)+a_{43,i}\left(a_{43,i}-a_{33,i}\right)\right]\left(\overline{w_{1,\iota}{}^2}-\overline{w_{1,\iota}w_{2,\iota}}\right)\end{matrix}}{\left(\begin{matrix}\left[a_{31,i}\left(a_{31,i}-a_{41,i}\right)+a_{33,i}\left(a_{33,i}-a_{43,i}\right)\right]\left[a_{42,i}\left(a_{42,i}-a_{32,i}\right)+a_{44,i}\left(a_{44,i}-a_{34,i}\right)\right]\\ -\left[a_{41,i}\left(a_{41,i}-a_{31,i}\right)+a_{43,i}\left(a_{43,i}-a_{33,i}\right)\right]\left[a_{32,i}\left(a_{32,i}-a_{42,i}\right)+a_{34,i}\left(a_{34,i}-a_{44,i}\right)\right]\end{matrix}\right)} \quad (17B)$$

Equations (17) quantify the noise associated with the longitudinal tristatic system (transceiver plus receivers 1 and 3) and the lateral tristatic system (transceiver plus receivers 2 and 4), respectively. They are more applicable to the Vectrino Profiler (and also the Vectrino) than the approach of Hurther and Lemmin (2001) and Blanckaert and Lemmin (2006), since angular variations imposed during manufacturing are explicitly included through use of the calibration matrix. In addition, although it is most likely that the noise variances of all beams are unequal, the assumption that the noise variances of opposite beams are equal is less restrictive than that imposed in previous work (e.g. Lohrmann *et al* 1995, Voulgaris and Trowbridge 1998, Hurther and Lemmin 2001). The resulting noise estimates can be combined with information held in the calibration matrix to estimate noise-corrected values of the variances, $\overline{u^2}$, $\overline{v^2}$, $\overline{w_1{}^2}$, $\overline{w_2{}^2}$, and $\overline{w_1 w_2}$, and covariances, $\overline{uv}$, $\overline{uw_1}$, $\overline{uw_2}$, $\overline{vw_1}$, and $\overline{vw_2}$, respectively.

4.2 Temporal convergence

The sampling period *T* necessary to yield given relative errors in the time averages, variances, $\overline{u^2}$, $\overline{v^2}$, and $\overline{w^2}$, and covariances, $\overline{uv}$, $\overline{uw}$, and $\overline{vw}$, may be estimated by first estimating the number of independent velocity samples, given by $T/2\tau$, where τ is the integral time scale of the local flow field given by integrating the temporal autocorrelation coefficient (Tennekes and Lumley 1972):

$$\tau_u = \int_0^\infty \frac{\overline{u(t)u(t+\Delta t)}}{\overline{u^2(t)}} d\Delta t \quad (18)$$

where the subscript u on τ explicitly recognises that the integral time scale for each velocity component, product and cross-product are not necessarily equal (Soulsby 1980) and Δt is a time delay. Note that equation (18) has been written for the u velocity component but can similarly be written for the v and w components. Combining equations given by Bendat and Piersol (1986: 288), Benedict and Gould (1996: 131), and Garcia *et al* (2006: 516), for a given relative root mean square error, ε, T may be estimated by:

$$T_{\overline{u}} \cong \frac{2\tau_u \overline{u^2}}{\varepsilon^2 \overline{u}^2} \quad (19A)$$

$$T_{\overline{u^2}} \cong \frac{2\tau_{\overline{u^2}}}{\varepsilon^2}\left[\frac{\overline{u^4}-\left(\overline{u^2}\right)^2}{\left(\overline{u^2}\right)^2}\right] \quad (19B)$$

$$T_{\overline{uv}} \cong \frac{2\tau_{\overline{uv}}}{\varepsilon^2}\left[\frac{\overline{u^2v^2}-(\overline{uv})^2}{(\overline{uv})^2}\right] \quad (19C)$$

where equations (19A)-(19C) have been written for $\bar{u}$, $\overline{u^2}$, and $\overline{uv}$, but again could be written for the other components. Note that we can expect that $T_{\overline{uv}} > T_{\overline{u^2}} > T_{\overline{u}}$ (e.g. Soulsby 1980). Confidence intervals on the time averages may be estimated using the standard deviations, a one-sided student's t table and setting the number of samples equal to, for example, $T/2\tau_u$, whereas confidence intervals on the (co)variances may be estimated using the (co)variances themselves, a two-sided student's t table and setting the number of samples equal to, for example, $\mathrm{T}/2\tau_{\overline{\mathrm{u}^2}}$ (Benedict and Gould 1996).

5 Results

5.1 Experiment 1: Sensitivity of amplitude and correlation to the concentration of acoustic seeding

Figures 4 and 5 show the impact of varying the concentration of acoustic seeding on the vertical variation of mean amplitude for 1 mm and 4 mm high cells, respectively. Mean amplitude varies parabolically, with a maximum at the sweet spot 50 mm below the transceiver and a reduction above and below that location, with a very slight decrease in the rate of reduction further away from the receiver (figure 4). This parabolic form is as expected, and is caused by the combination of the smoothly varying nature of the received signal and the vertical variation

of the bistatic angle. As the concentration of acoustic seeding is increased, the pattern of change becomes smoother, the maximum gets larger, the peak is broadened (i.e., the sweet spot is lengthened) and the reduction of amplitude above the sweet spot is lessened (figure 4). The spatial variability for 4 mm high cells is similar to that for 1 mm high cells, but the increased spatial averaging results in less attenuation of mean amplitude, especially towards the top of the profile (figure 5).

These spatial trends have a strong influence on the vertical variation of the correlation coefficient (figures 6 and 7). In particular, there is a significant decrease in correlation for concentrations < 3,000 mg L^{-1} (figure 6). Interestingly, correlation is increased at the sweet spot at low-to-medium concentrations and actually decreases for higher concentrations (figures 6 and 7), with an optimum concentration of seeding of between 3,000 and 6,000 mg L^{-1}. Scattering and attenuation become significant at concentrations > 20,000 mg L^{-1}, effectively modifying the geometry shown in figure 1 and invalidating the calibration (A. Lohrmann, personal communication, 22nd October, 2015). In addition, correlation is generally larger above the sweet spot for 4 mm high cells than for 1 mm high cells but it is generally smaller below the sweet spot for 4 mm high cells than for 1 mm high cells (figures 6 and 7). Consideration of the form of the correlation profiles suggests that reliable velocity data are most likely to be collected in the region between 43 and 60 mm below the transceiver, with less reliable data more likely with greater distance from this region, and that reliability will degrade further for lower concentrations of acoustic scatterers.

5.2 Experiment 2: Internal consistency of velocities and noise in neighbouring cells in a single profile at a range of transceiver power settings and seeding concentrations

Figure 8(a) illustrates the vertical variation of mean streamwise velocity with cell number, measured at a constant height of 30 mm above the flume floor, for a range of power settings. It is apparent that, contrary to expectation, mean streamwise velocity is not constant with cell number and varies by ±10%, despite the absolute position of the sampling volume remaining constant (figure 8(a)). For all power settings and seeding concentrations, higher velocity magnitudes were recorded at proximal cells than at the sweet spot, while lower magnitudes were recorded at distal cells than at the sweet spot (figure 8(a)). The same trends are present for measurements repeated with the probe oriented at 90° and 180° to the flume channel axis at 'high' power and saturated seeding concentrations (note that in all cases, velocities have been transformed so that they have the same direction as the measurement

undertaken at 0°) (figure 8(a)). The 90° and 180° rotated series highlight that the velocity magnitude is biased, i.e. distal cells are biased towards zero irrespective of whether positive or negative velocities are measured (figure 8(a)). The impact of the power setting on velocity bias is most significant for the distal cells when using 'low' power settings and 'clear' water conditions (figure 8(a)).

Figure 8(b) shows the vertical variation with cell number of noise on the longitudinal tristatic system, estimated using equation (17A), measured at a constant height of 30 mm above the flume floor, for a range of power settings. Noise varies parabolically, increasing from a minimum at the sweet spot to cells that are proximal and distal to the transceiver (figure 8(b)). For the high power setting, noise is larger in distal cells than lower power settings, whereas the power setting does not appear to impact upon noise in proximal cells (figure 8(b)). Adding kaolin reduces noise but probe orientation does not have a consistent effect on noise. Note that the longitudinal tristatic system at an orientation of 90° is the lateral tristatic system at an orientation of 0° and the lateral tristatic system at an orientation of 90° is the longitudinal tristatic system at an orientation of 0°. Figure 8(d) shows the vertical variation of noise on the lateral tristatic system, estimated using equation (17B). The noise on the lateral tristatic system is 33-50% of the noise on the longitudinal tristatic system, and exhibits significantly less variation than the noise on the longitudinal tristatic system (figure 8(d)). The parabolic form can be explained by the vertical variation of SNR (figure 8(c)), which has a maximum at the sweet spot and then reduces to cells that are proximal and distal to the transceiver. SNR is defined as signal amplitude minus noise amplitude (equation 12). But, following Zedel (2008), the signal amplitude contains both the true signal due to coherent backscatter and incoherent backscatter caused by temporal variations (i.e., random (turbulent) motions) and changes in backscatter strength caused by beam divergence and mean velocity gradients in the sampling volume (Voulgaris and Trowbridge 1998, McLelland and Nicholas 2000). Thus, σ_{13}^2 and σ_{24}^2 equate to the sum of the noise due to incoherent backscatter and the noise amplitude for the longitudinal and lateral tristatic systems, respectively; for a given power level, σ_{13}^2 and σ_{24}^2 must be inversely proportional to SNR. Furthermore, since the noise amplitude can be assumed constant for given seeding concentrations, it is unsurprising that SNR increased with increasing power level (figure 8(c)). Similarly, adding kaolin increased SNR further, but had the largest effect when the probe was oriented at 0° to the flume axis (figure 8(c)). Consideration of figures 8(b) and 8(c) implies a threshold SNR above which the effects of noise can be minimised. This threshold varies from about 25 dB at the sweet spot to about 35 dB in proximal and distal cells.

These values are significantly more conservative than those recommended by Nortek (NortekUSA 2013, MacVicar *et al* 2014).

5.3 Experiment 3: Internal consistency of velocities and noise in neighbouring cells in a single profile under optimal seeding conditions

Figure 9a illustrates the vertical variation of mean streamwise velocity with cell number, measured at a constant height of 30 mm above the flume floor, for a range of ambiguity velocities and a pump setting of 10 Hz. This pump setting yielded a mean streamwise velocity of 0.105 m s^{-1} at the sweet spot. As in figure 8(a), mean streamwise velocity was not constant with cell number, and varied by ±10% despite the absolute position of the sampling volume remaining constant (figure 9(a)). However, the form of that variation is not the same as that exhibited by the probe that collected the data in figure 8(a), with velocity magnitudes similar to those at the sweet spot recorded in proximal cells and lower velocity magnitudes recorded in distal cells than at the sweet spot (figure 9(a)). Ambiguity velocity does not appear to have a significant impact upon the mean streamwise velocity, since the selected ambiguity velocities prevented any aliasing.

Figure 9(b) shows the vertical variation with cell number of noise, normalised by the noise-free variance of the vertical velocity, on the longitudinal tristatic system, estimated using equation (17A), measured at a constant height of 30 mm above the flume floor. Similar to the form exhibited by the probe that was used to collect the data in figure 8(b), noise varies parabolically, increasing from a minimum at the sweet spot to cells that are proximal and distal to the transceiver (figure 9(b)). Figure 9(d) shows the vertical variation of noise, normalised by the noise-free variance of the vertical velocity, on the lateral tristatic system, estimated using equation (17B). In contrast to the probe that was used to collect the data in figure 8, the noise on the lateral tristatic system is only marginally less than the noise on the longitudinal tristatic system, and exhibits a similar parabolic form (figure 9(d)). The parabolic form can again be explained by the vertical variation of SNR (figure 9(c)), which has a maximum at the sweet spot and then reduces to cells that are proximal and distal to the transceiver (figure 9(c)). In both figures 9(b) and 9(d), it is noticeable that noise distal to the transceiver is significantly larger for the case when the ambiguity velocity was 0.343 m s^{-1}. This ambiguity velocity invoked the dual pulse-pair repetition scheme, which is inherently noisier than the single pulse-pair scheme (e.g., Holleman and Beekhuis 2003, Joe and May 2003).

Figure 10(a) illustrates the vertical variation of mean streamwise velocity with cell number, measured at a constant height of 30 mm above the flume floor, for a range of ambiguity velocities and a pump setting of 25 Hz. This pump setting yielded a mean streamwise velocity of 0.30 m s^{-1} at the sweet spot. As in figures 8(a) and 9(a), mean streamwise velocity was not constant with cell number, and varied by ±10% despite the absolute position of the sampling volume remaining constant (figure 10(a)). The form of the variation matched that in figure 9(a), with velocity magnitudes similar to those at the sweet spot recorded in proximal cells and lower velocity magnitudes recorded in distal cells than at the sweet spot (figure 10(a)). Once again, ambiguity velocity does not appear to have a significant impact upon the mean streamwise velocity, since the selected ambiguity velocities prevented any phase wrapping.

Figures 10(b) and 10(d) show the vertical variation with cell number of noise, normalised by the noise-free variance of the vertical velocity, on the longitudinal and lateral tristatic systems, respectively, estimated using equations (17A) and (17B), respectively. Noise varied parabolically and with a similar magnitude relative to the variance of the vertical velocity as that shown in figures 9(b) and 9(d); both the noise components and $\overline{w_1 w_2}$ were 6-7 times larger for the cases in figure 10 than those in figure 9. SNR was almost identical for the two sets of experiments (figures 9(c) and 10(c)). Voulgaris and Trowbridge (1998) and McLelland and Nicholas (2000) showed that noise contains contributions from both Doppler broadening and the mean velocity gradient in the sampling volume. The dominant component of Doppler broadening is due to turbulence and is assumed proportional to the cube root of the turbulence dissipation rate (Voulgaris and Trowbridge 1998) or the root mean square (rms) of the on-axis radial velocity (= beam velocity, McLelland and Nicholas 2000), which may be approximated by the rms of the vertical velocity. However, the rms of the vertical velocity, $\overline{w_1 w_2}^{1/2}$, was only 2-3 times larger for the cases in figure 10 than those in figure 9, implying that the noise terms are not proportional to rms for these cases. In contrast to figures 9(b) and 9(d), the noise for an ambiguity velocity of 0.343 m s^{-1} (dual pulse-pair algorithm) was not significantly greater than that of an ambiguity velocity of 0.185 m s^{-1} (single pulse-pair algorithm) (figures 10(b) and 10(d)), which implies that Doppler broadening is not the dominant component of the noise associated with the dual pulse-pair algorithm.

Figure 11 illustrates the vertical variation of the time-averaged beam velocities with position number, measured at a constant height of 30 mm above the flume floor, for a range of ambiguity velocities and pump settings of 10 Hz (figure 11(a)) and 25 Hz (figure 11(b)), respectively. It is clear that beam velocities are also not constant with cell number and vary by

±10-16%, with magnitudes that are larger proximal to the transceiver and smaller distal to the transceiver (figure 11). The lack of symmetry of V_{b2} and V_{b4} about a velocity of 0 m s^{-1} implies that there was slight misalignment of the probe with the flume axis (figure 11). In addition, deviations of V_{b1} from its otherwise near-linear trend in the vertical are not necessarily reflected in deviations of V_{b3} and deviations of V_{b2} from its otherwise near-linear trend in the vertical are not necessarily reflected in deviations of V_{b4}; note especially the disparity in behaviour proximal to the transceiver (figure 11). Furthermore, for the 25 Hz case (figure 11(b)), there appears to be a waviness superimposed upon an otherwise linear decrease of V_{b3} from proximal to distal. Ambiguity velocity does not appear to have a significant impact upon the time-averaged beam velocities, since the selected ambiguity velocities prevented any aliasing (figure 11).

5.4 Assessment of the noise correction method (equations (17))

Figure 12 compares the effectiveness of the noise correction method derived herein (equations (17)) against that of Hurther and Lemmin (2001) for the clear water, high power case of Experiment 2. All subplots show the vertical variation of noise-related variables with cell number, measured at a constant height of 30 mm above the flume floor. While equations (17) provide noise estimates for both the longitudinal and lateral tristatic systems, σ_{13}^2 and σ_{24}^2, the Hurther and Lemmin (2001) method averages the noise over all receivers (figure 12(a)) and sets $\sigma^2 = \left(\overline{w_1^2} + \overline{w_2^2} - 2\overline{w_1 w_2}\right)/2$ (Blanckaert and Lemmin 2006). σ^2 is overdetermined because σ^2 can be estimated by imposing that any of $\overline{\widehat{w_1}^2}$, $\overline{\widehat{w_2}^2}$ or $\overline{\widehat{w_1 w_2}}$ are equal. This overdetermination means that, while equations (17) rigorously impose $\overline{w_1^2} = \overline{w_2^2} = \overline{w_1 w_2}$ throughout the profile, the method of Hurther and Lemmin (2001) cannot (figure 12(b)). Therefore, although the Hurther and Lemmin (2001) method reduces the noise on $\overline{w_1^2}$ and $\overline{w_2^2}$, it does not change the relative difference $\left(\overline{w_1^2} - \overline{w_2^2}\right)/\overline{w_1 w_2}$. This is because, under the assumption of identical and ideal receivers, the noise corrections for $\overline{w_1^2}$ and $\overline{w_2^2}$, $(a_{31}^2 + a_{33}^2)\sigma^2$ and $(a_{42}^2 + a_{44}^2)\sigma^2$, respectively, are equal and thus cancel. The inability to impose $\overline{w_1^2} = \overline{w_2^2} = \overline{w_1 w_2}$ is especially relevant for the distal cells of the profile, where the noise on the two orthogonal tristatic systems differs considerably (figure 12(a)), emphasising that the assumption of equal noise on all receivers is not valid. Figures 12(c) and 12(d) show that equations (17) apply a larger correction to the longitudinal tristatic system (figure 12(c)) and a smaller correction to the lateral tristatic system (figure 12(d)), but the Hurther and

Lemmin (2001) method applies an equal correction to both systems. This is insignificant at the sweet spot, where both methods provide similar noise estimates, but may be important in proximal and distal cells where the Hurther and Lemmin (2001) method may underestimate the noise on one system and overestimate it on the other. For our example case, if it assumed that $\overline{u^2}$ and $\overline{v^2}$ are least noisy at the sweet spot (e.g. Brand *et al* 2016), equations (17) provide significantly improved noise estimates for $\overline{u^2}$ relative to the Hurther and Lemmin (2001) method (figure 12(c)). For $\overline{v^2}$, equations (17) provide similar noise estimates to the Hurther and Lemmin (2001) method in proximal cells to 58 mm below the transceiver but underestimate noise in distal cells (figure 12(d)).

6 Discussion

This section explores two key observations. First, mean velocities sampled by the Vectrino Profiler are biased, such that velocity magnitudes are biased by variable amounts in cells proximal to the transceiver, while velocity magnitudes are consistently underestimated in cells distal to the transceiver (figures 8-10(a) and 11). Second, vertical profiles of the noise on the longitudinal and lateral tristatic systems, σ_{13}^2 and σ_{24}^2, respectively, are parabolic with a minimum at the sweet spot (figures 8-10(b) and (d)), where signal amplitude, SNR and R^2 all reach their maxima (figures 4-6).

6.1 Bias in mean velocity estimates

Since the release of the Vectrino Profiler in 2010, many scientists (e.g., Zedel and Hay 2011, Ursic *et al* 2012, MacVicar *et al* 2014) and many users who have posted on the knowledge center section of Nortek's website (http://www.nortek-as.com/en/knowledge-center/forum/vectrinoii) have reported that overlapping mean velocity and variance and covariance profiles do not match perfectly. Since (assumed random) noise does not contribute to mean velocity estimates, noise cannot explain the bias on mean velocities. The extent of the bias varies for different probes (compare figures 8-10(a)), which implies that either the quality of individual probes varies or the calibration that transforms beam velocities to orthogonal velocities differs in quality. Figure 11 shows that beam velocities are not constant with cell number and vary by ±10-16%, with magnitudes that are larger proximal to the transceiver, smaller distal to the transceiver and waviness superimposed over the otherwise linear trend (figure 11(b)). This implies that bias is inherent to the probe geometry and that such bias cannot

be removed by a transformation matrix that varies linearly with distance from the transceiver (contrast this with the ADVP of Hurther and Lemmin, 2001). Figures 9-10(a) and 11 show that rather than removing bias, application of the transformation matrix propagates that bias and imposes additional curvature on streamwise velocity profiles. Lohrmann (personal communication, 22nd October, 2015) reported that the calibration procedure that had initially been implemented by Nortek, towing a probe at ±0.2 m s^{-1} in a tank of relatively limited dimensions, made invalid assumptions about the flow field around the probe. Specifically, he showed that the probe head deflects flow when it is towed, which explains why the calibration varied with tow velocity (Ursic *et al* 2012). In response to this, together with the observation that velocities outputted by the Vectrino Profiler were in error by an average of 1.5% and a maximum of 5% at a tow speed of ±0.6 m s^{-1}, Nortek modified the calibration procedure in May 2016 so that it is now undertaken by towing a probe at ±0.2, ±0.5 and ±0.8 m s^{-1} in a 10 m long × 10 m wide × 2 m deep tank and performing an unweighted least squares adjustment (A. Lohrmann, personal communication, 22nd October, 2015). However, it is our understanding that this procedure is not repeated with the probes rotated 90°, implying that the calibration is likely to be more robust in the longitudinal direction than in the lateral direction. Nevertheless, Lohrmann (personal communication, 25th April, 2016) reported that the improved calibration procedure removes curvature in velocity profiles. It is stressed that this:

1. is only possible if the coefficients of the transformation matrices, especially those of beams 1 and 3, which are likely to have been most impacted by wake effects during the calibration procedure, vary nonlinearly;
2. implicitly accepts that the calibration matrices vary with velocity, such that fast and slow velocities will be biased in opposite directions (i.e. underestimates at slow velocities and overestimates at fast velocities or overestimates at slow velocities and underestimates at fast velocities, respectively). As of the publication date, Nortek had commenced providing a calibration report to users detailing these biases.

At the time of writing, it has not been possible to repeat experiments 1, 2 and 3 for a recalibrated probe. However, figure 13 compares the coefficients of the transformation matrix, a_{ij} (equation (13B)), as originally supplied and following recalibration by Nortek, for an example probe (probe and hardware serial numbers VCN8773 and VNO1468, respectively). The vertical variation of the calibration coefficients is compared against the theoretical values obtained from equation (13C). The coefficients that dominate the transformation from beam velocities to *u* and *v* deviate from the theoretical curve by a maximum of ±1% until cell 27, or a range of 66 mm below the transceiver for both sets of calibration coefficients (figures 13(a)

and 13(b)). However, recalibration significantly reduced the cross-tristatic system coefficients (figure 13(c)) and the coefficients that dominate the transformation from beam velocities to w_1 and w_2 (figure 13(d)), such that they are all much closer to their theoretical values and a_{32}, a_{34}, a_{42}, and a_{44} are equal to their theoretical values. Noise multipliers (not shown) are not changed significantly.

6.2 Parabolic noise profiles

As noted, vertical profiles of the noise on the longitudinal and lateral tristatic systems, σ_{13}^2 and σ_{24}^2, respectively, are parabolic with a minimum at the sweet spot (figures 8-10(b) and (d)), where signal amplitude, SNR and R^2 all reach their maxima (figures 4-6). Zedel (2008, 2015) presented a probabilistic acoustic backscatter model and used it to quantify the form of the intersection of the transceiver and receiver beams of a prototype bistatic system and the Vectrino Profiler. Brand *et al* (2016) drew a schematic of the sampling volume of the Vectrino Profiler and noted the changing area of overlap of the acoustic beams of the transceiver and receivers. Herein, the geometry of the Vectrino Profiler, together with the assumption that all particles that have an equal path length and lie within the intersection of the transceiver and receiver beams are sampled simultaneously by the Vectrino Profiler, is used to estimate the shape and size of the sampling cells of the Vectrino Profiler. This approach is less complex than the model of Zedel (2008, 2015), but it is deterministic and permits the quantitative description of the behaviour of the instrument.

To perform these calculations, it is necessary to know the initial position, width and spreading angle of the acoustic beams (transceiver and receivers). The outermost edge of each receiver arm is a horizontal distance of 30.25 mm and a vertical distance of 7.9 mm from the centre of the transceiver face (Nortek 2015b). Receivers are located on the centreline of the receiver arm and it is assumed that the outermost edge of each receiver occurs 2 mm from the end of the receiver arm. The initial width of the transceiver beam is defined by the diameter of the ceramic disc transducer (6 mm, Nortek 2015b). The receiver beams are also assumed to have an initial width of 6 mm (Nortek 2015b, Zedel 2015). For the Vectrino Profiler, the spreading angles have not been published. Since the calibrated profiling range of the Vectrino Profiler is 40-74 mm, this knowledge can be used to select an appropriate spreading angle for both the transceiver and the receivers, under the assumption that they are identical for all beams and the beams must intersect to yield a finite cell volume. Such a pre-calculation yields a maximum spreading angle of 3.0°. Support for the use of this value is given by considering the

transceivers of ADCP probes manufactured by Nortek, which have transceiver spreading angles of 1.7° to 3.7° (Nortek 2015b).

Let us now consider the shape of cell volumes in the vertical plane lying through the transceiver and beams 1 and 3 (or, equivalently, beams 2 and 4). By definition, the sampling volume of a particular cell is formed by the initial (x, y, z) position of suspended particles for which the total distance, or time, of travel of an emitted pulse from the transceiver to the particle and back to a receiver is equal. The sampling volumes are therefore ellipsoidal in shape. For example (see figure 14), assuming 1 mm cells, cell 1 is centred 40 mm from the transceiver and its sampling volume is formed by the region bounded by the ellipses with tangents 39.5 and 40.5 mm beneath the transceiver and the margins of the transceiver and receiver beams (figure 14). For cell 1, the relevant region is the uppermost red area in figure 14. To determine the extent of the next cell, all points that lie within a 1 mm longer path length are considered, and so on to the last cell (figure 14). The centre of mass (centroid) of each cell is demarcated by circles; the centroid of each cell defined by the transceiver and opposite receiver is demarcated by crosses (figure 14). The locations of all the cell centroids are presented in table 2.

The estimated longitudinal locations of the centroids are in close correspondence with expectation, i.e. ranging from 40 mm to 74 mm in steps of 1 mm. Moreover, the cell centroids are approximately located on a straight line making a 15° angle with the vertical, corresponding to the angle of the bisector, $\beta/2$, that forms an approximate axis of symmetry. The cells having the largest measurement volumes and centroids closest to the central axis of the transceiver are those located between 48 mm and 50 mm from the transceiver (figure 14, table 2). These correspond to the sweet spot, or equivalently the intersection of the central axes of the transceiver and receivers. Conversely, table 2 shows that the lateral mismatch between receivers comprising a tristatic system exceeds the diameter of the original transmitted beam width in cells 21 to 35. This mismatch, together with reductions in cell volume, causes R^2 and SNR to decrease significantly from 61 mm to 74 mm below the transceiver, even under optimal seeding conditions (figures 6 and 7). Reduced SNR causes increased velocity variance and therefore velocities sampled at cells other than the sweet spot inherently have elevated measurement error (*cf.* Miller and Rochwarger 1972, Zrnic 1977, McLelland and Nicholas 2000, Zedel 2008), associated with the reduction of acoustic energy towards the edges of the transmitted acoustic beam. Conversely, the aspect ratio (cell width: cell height) is largest at the sweet spot and decreases away from the sweet spot, which causes the averaging of turbulent

flow structures over a considerably larger lateral distance than might be expected. The impact of this effect may be reduced somewhat by selecting larger cell heights.

Comparing against the acoustic backscatter model of Zedel (2015), cell locations match well between 40 mm and 64 mm below the transceiver (+2.2 and −4.1 mm, respectively, table 2), but diverge significantly in distal cells, where the model of Zedel (2015) predicts that SNR falls to near zero and cell locations are rather uncertain. The lateral offset of the centroids of the cells of paired receivers (table 2) is critical to this discussion. This offset is not accounted for when transforming beam velocities into three-component velocities, which causes an additional source of error. Although the resulting error introduces bias into mean three-component velocities (see figures 8(a) and 9(a)), it will have the greatest impact upon higher order flow statistics and is expected to be largest for flows with velocity gradients, where the (mean) velocity differs between the cell centres of the co-planar receivers. Furthermore, the lateral offset introduces significant complications when velocities (largely) derived from perpendicular beam pairs are multiplied to form covariances (e.g. $\overline{uv}$, $\overline{uw_2}$, and $\overline{vw_1}$) and variance $\overline{w_1 w_2}$ (Brand *et al* 2016) or to compute auto- or co-spectra. Brand *et al* (2016) describe the resulting decorrelation and underestimated (co)variance and thus recommend the use of $\overline{uw_1}$ and $\overline{vw_2}$ in preference to $\overline{uw_2}$ and $\overline{vw_1}$, respectively. Although $\overline{w_1 w_2}$ is affected by this problem, which may hinder application of the noise removal technique of Hurther and Lemmin (2001) or that derived herein, it must also be recognised that $\overline{{w_1}^2}$ and $\overline{{w_2}^2}$ are orders of magnitude noisier than $\overline{w_1 w_2}$ (table 1).

In an attempt to reduce the impact of noise on the variances and covariances quantified by the Vectrino Profiler, in May 2016 Nortek changed their production procedure to use half-size receiver ceramics in the Vectrino Profiler probe, which makes the response curve “flatter” (i.e., the reduction of SNR through the profile is much smaller than previously: about 6 dB from the sweet spot to both proximal and distal cells) and makes the probe less susceptible to variations of the spherical scattering function of the particles that scatter sound (A. Lohrmann, personal communication, 25th April, 2016). It is assumed that the smaller receiver ceramics also have a narrower beam spreading angle, which has resulted in a shorter calibrated profiling range (a maximum of 40 to 70 mm). The choice to switch to smaller, more focussed receivers is an interesting one, and is diametrically opposed to the approach of Hurther and Lemmin (1998), who employ large angle receivers with their longest axis perpendicular to the receiver arm. At the time of writing, it has not been possible to assess whether the redesigned receivers yield improved data quality.

7 Conclusion

This paper provides a comprehensive explanation of Nortek Vectrino Profiler operation and explains the behaviour, accuracy and precision of the instrument prior to the introduction of modified receiver ceramics and a modified calibration procedure in May 2016. In achieving this, it has:

1. explained the operating principles of the Vectrino Profiler and the influence of user-selectable parameters such as cell size, velocity range, and ping algorithm, on data quality;
2. employed a novel methodology to highlight the inherent bias in mean velocity estimates made with a Vectrino Profiler. Velocity magnitudes are biased by variable amounts in proximal cells, but are consistently underestimated in distal cells (figures 8-10(a)). Others (e.g., Zedel and Hay 2011, Ursic *et al* 2012, MacVicar *et al* 2014) have previously reported that overlapped profiles do not match perfectly. Since (assumed random) noise does not contribute to the mean value, noise cannot explain this bias. The extent of the bias is a function of the quality of individual probes and the calibration that transforms beam velocities to orthogonal velocities;
3. shown that when 1 mm cells are employed, amplitude (and thence signal-to-noise ratio, SNR) profiles are parabolic with a maximum at or near the "sweet spot", 50 mm below the transceiver (figure 4). When 4 mm cells are employed, amplitude and SNR profiles decline smoothly from a broad peak between the sweet spot and the top of the profile to distal cells (figure 5);
4. investigated the influence of acoustic scatterer concentration (seeding) on amplitude and SNR (figures 4 and 5), and furthermore on correlation (R^2, figures 6 and 7), for idealised, well-distributed seeding. R^2-values increase and become more consistent as concentrations increase to an optimum level of ~3,000 to 6,000 mg L^{-1}, but decline at higher concentrations, especially for larger cell sizes and distal to the transceiver. This is because of signal saturation, increased scattering and attenuation. It is stressed that for the idealised conditions explored herein, seeding concentrations between 6,000 and 20,000 mg L^{-1} still yielded outstanding mean R^2 values (>94%), so that concentrations in this range should not be considered overly detrimental to data quality. Sensitivity to higher seeding particle concentrations may differ for different particle types and under sub-optimal seeding conditions, e.g. in field experiments;

5. derived a new solution (equations (17)) for quantifying the noise on the two perpendicular tristatic systems formed by the transceiver and receivers 1 and 3 and the transceiver and receivers 2 and 4, respectively. This solution improves upon previous results (Hurther and Lemmin 2001), since it permits different estimates of noise for the longitudinal tristatic system, σ_{13}^2, and the lateral tristatic system, σ_{24}^2, (see figures 8-10(b) and (d)) which was reported by Brand *et al* (2016). Thus, it is possible to account for variations in the build quality of probes. In addition, the solution derived herein does not assume that covariances are noise free. Brand *et al* (2016) further attribute the difference in the noise estimates, σ_{13}^2 and σ_{24}^2, to Doppler noise, which increases with either the cube root of the turbulence dissipation rate (Voulgaris and Trowbridge 1998) or the root mean square of the on-axis beam velocity (McLelland and Nicholas 2000). Thus, in flume experiments where flow is predominantly in the longitudinal (streamwise) direction, $\sigma_{13}^2 > \sigma_{24}^2$ (figures 8-10(b) and (d)). However, in the experiments reported herein (figures 9 and 10(b) and (d)), σ_{13}^2 and σ_{24}^2 scaled with the (noise-free) variance of the vertical velocity (which approximates the variance of the on-axis beam velocity). Nevertheless, the dependence of Doppler noise on turbulence, as observed by many others including Hurther and Lemmin (2001) and Brand *et al* (2016), explains the higher noise levels at faster flow velocities (compare figures 9 and 10(b) and (d));
6. confirmed that noise propagates strongly into estimates of the variances, $\overline{u^2}$, $\overline{v^2}$, $\overline{{w_1}^2}$, and $\overline{{w_2}^2}$ (see also Hurther and Lemmin 2001, Blanckaert and Lemmin 2006, Brand *et al* 2016), but weakly into the covariances $\overline{uv}$, $\overline{uw_1}$, $\overline{uw_2}$, $\overline{vw_1}$, and $\overline{vw_2}$. Conversely, $\overline{w_1 w_2}$ is virtually noise free, as assumed by Hurther and Lemmin (2001). Profiles of σ_{13}^2 and σ_{24}^2 were shown to be parabolic, which explains the form of $\overline{u^2}$ profiles observed by Zedel and Hay (2011) and provides an explanation for the apparent error in profiles of $\overline{u^2}^{1/2}$ reported by MacVicar *et al* (2014). Although Brand *et al* (2016) showed that the method of Hurther and Lemmin (2001) can remove a large fraction of the noise included in the variances, the solution for estimating noise derived herein may also be used to remove noise from the variances and covariances (table 1). This conclusion may be validated through direct comparison against independent measurements undertaken with an alternative method (e.g., as performed with LDV for a non-profiling ADV, Voulgaris and Trowbridge 1998);

7. explained how the probe geometry causes the four receivers to intersect at a single location in the vertical (the sweet spot), where the sampling volume is largest, but that the geometry of the receivers causes spatial divergence of the sampled position both proximal and distal to the transceiver (figure 13). This spatial divergence yields a significant reduction in the size of the sampled area and a decrease in SNR, resulting in reduced data quality proximal and distal to the transceiver. This, combined with consideration of the form of R^2 profiles, suggests that reliable velocity data are most likely to be collected in the region between 43 and 61 mm below the transceiver;
8. highlighted the fact that the bias inherent in estimates of the second order flow statistics may be reduced but cannot be removed with sensor improvements, since Doppler noise is to a large extent a function of the flow field. A revised calibration procedure may reduce bias in mean velocity estimates but it is unlikely to entirely remove it.

Declaration of interest

We wish to confirm that there are no known conflicts of interest associated with this publication and there has been no significant financial or in-kind support for this work that could have influenced its outcome.

Acknowledgements

We wish to thank Dr. Chris Unsworth for undertaking the tests described and reported in sections 4.1 and 6.1 while he undertook PhD studies at the University of Hull. We are also grateful to the technical staff of the Hydraulics Laboratory at Ghent University for constructing the experimental setup described in sections 4.2 and 6.2. In addition, we wish to acknowledge Atle Lohrmann of Nortek AS and Robert Craig of Nortek Scientific, who have accommodated myriad requests for information about the Vectrino Profiler. RET wishes to thank the Institute of Applied Geosciences at the School of Earth and Environment at the University of Leeds for financial assistance that enabled attendance of the Nortek European User Symposium that was held in Karlsruhe, Germany, in October 2015, LS is grateful to the Research Foundation - Flanders for funding his Ph.D. fellowship, while SC is grateful to the Special Research Fund (BOF) of Ghent University for funding his Ph.D. fellowship. The tests described and reported in sections 4.3 and 6.3 were supported in part by the European Community's 7th Framework Programme through a grant to the budget of the Integrated Infrastructure Initiative HYDRALAB IV, Contract no. 261520.

Appendix

Equations for the velocity variances and covariances are given in this section. Circumflexes denote noise-free terms.

$$\overline{u_\iota^2} = a_{11,i}^2\left(\overline{\widehat{V_{b1,\iota}}^2} + \sigma_{13,i}^2\right) + a_{12,i}^2\left(\overline{\widehat{V_{b2,\iota}}^2} + \sigma_{24,i}^2\right) + a_{13,i}^2\left(\overline{\widehat{V_{b3,\iota}}^2} + \sigma_{13,i}^2\right) + a_{14,i}^2\left(\overline{\widehat{V_{b4,\iota}}^2} + \sigma_{24,i}^2\right) + 2a_{11,i}a_{12,i}\overline{\widehat{V_{b1,\iota}}\widehat{V_{b2,\iota}}} + 2a_{11,i}a_{13,i}\overline{\widehat{V_{b1,\iota}}\widehat{V_{b3,\iota}}} + 2a_{11,i}a_{14,i}\overline{\widehat{V_{b1,\iota}}\widehat{V_{b4,\iota}}} + 2a_{12,i}a_{13,i}\overline{\widehat{V_{b2,\iota}}\widehat{V_{b3,\iota}}} + 2a_{12,i}a_{14,i}\overline{\widehat{V_{b2,\iota}}\widehat{V_{b4,\iota}}} + 2a_{13,i}a_{14,i}\overline{\widehat{V_{b3,\iota}}\widehat{V_{b4,\iota}}} \quad \text{(A1)}$$

$$\overline{u_\iota v_\iota} = a_{11,i}a_{21,i}\left(\overline{\widehat{V_{b1,\iota}}^2} + \sigma_{13,i}^2\right) + a_{12,i}a_{22,i}\left(\overline{\widehat{V_{b2,\iota}}^2} + \sigma_{24,i}^2\right) + a_{13,i}a_{23,i}\left(\overline{\widehat{V_{b3,\iota}}^2} + \sigma_{13,i}^2\right) + a_{14,i}a_{24,i}\left(\overline{\widehat{V_{b4,\iota}}^2} + \sigma_{24,i}^2\right) + \left(a_{11,i}a_{22,i} + a_{12,i}a_{21,i}\right)\overline{\widehat{V_{b1,\iota}}\widehat{V_{b2,\iota}}} + \left(a_{11,i}a_{23,i} + a_{13,i}a_{21,i}\right)\overline{\widehat{V_{b1,\iota}}\widehat{V_{b3,\iota}}} + \left(a_{11,i}a_{24,i} + a_{14,i}a_{21,i}\right)\overline{\widehat{V_{b1,\iota}}\widehat{V_{b4,\iota}}} + \left(a_{13,i}a_{22,i} + a_{12,i}a_{23,i}\right)\overline{\widehat{V_{b2,\iota}}\widehat{V_{b3,\iota}}} + \left(a_{12,i}a_{24,i} + a_{14,i}a_{22,i}\right)\overline{\widehat{V_{b2,\iota}}\widehat{V_{b4,\iota}}} + \left(a_{13,i}a_{24,i} + a_{14,i}a_{23,i}\right)\overline{\widehat{V_{b3,\iota}}\widehat{V_{b4,\iota}}} \quad \text{(A2)}$$

$$\overline{u_\iota w_{1,\iota}} = a_{11,i}a_{31,i}\left(\overline{\widehat{V_{b1,\iota}}^2} + \sigma_{13,i}^2\right) + a_{12,i}a_{32,i}\left(\overline{\widehat{V_{b2,\iota}}^2} + \sigma_{24,i}^2\right) + a_{13,i}a_{33,i}\left(\overline{\widehat{V_{b3,\iota}}^2} + \sigma_{13,i}^2\right) + a_{14,i}a_{34,i}\left(\overline{\widehat{V_{b4,\iota}}^2} + \sigma_{24,i}^2\right) + \left(a_{11,i}a_{32,i} + a_{12,i}a_{31,i}\right)\overline{\widehat{V_{b1,\iota}}\widehat{V_{b2,\iota}}} + \left(a_{11,i}a_{33,i} + a_{13,i}a_{31,i}\right)\overline{\widehat{V_{b1,\iota}}\widehat{V_{b3,\iota}}} + \left(a_{11,i}a_{34,i} + a_{14,i}a_{31,i}\right)\overline{\widehat{V_{b1,\iota}}\widehat{V_{b4,\iota}}} + \left(a_{13,i}a_{32,i} + a_{12,i}a_{33,i}\right)\overline{\widehat{V_{b2,\iota}}\widehat{V_{b3,\iota}}} + \left(a_{12,i}a_{34,i} + a_{14,i}a_{32,i}\right)\overline{\widehat{V_{b2,\iota}}\widehat{V_{b4,\iota}}} + \left(a_{13,i}a_{34,i} + a_{14,i}a_{33,i}\right)\overline{\widehat{V_{b3,\iota}}\widehat{V_{b4,\iota}}} \quad \text{(A3)}$$

$$\overline{u_\iota w_{2,\iota}} = a_{11,i}a_{41,i}\left(\overline{\widehat{V_{b1,\iota}}^{\,2}} + {\sigma_{13,i}}^2\right) + a_{12,i}a_{42,i}\left(\overline{\widehat{V_{b2,\iota}}^{\,2}} + {\sigma_{24,i}}^2\right) + a_{13,i}a_{43,i}\left(\overline{\widehat{V_{b3,\iota}}^{\,2}} + {\sigma_{13,i}}^2\right) + a_{14,i}a_{44,i}\left(\overline{\widehat{V_{b4,\iota}}^{\,2}} + {\sigma_{24,i}}^2\right) + \left(a_{11,i}a_{42,i} + a_{12,i}a_{41,i}\right)\overline{\widehat{V_{b1,\iota}}\widehat{V_{b2,\iota}}} + \left(a_{11,i}a_{43,i} + a_{13,i}a_{41,i}\right)\overline{\widehat{V_{b1,\iota}}\widehat{V_{b3,\iota}}} + \left(a_{11,i}a_{44,i} + a_{14,i}a_{41,i}\right)\overline{\widehat{V_{b1,\iota}}\widehat{V_{b4,\iota}}} + \left(a_{13,i}a_{42,i} + a_{12,i}a_{43,i}\right)\overline{\widehat{V_{b2,\iota}}\widehat{V_{b3,\iota}}} + \left(a_{12,i}a_{44,i} + a_{14,i}a_{42,i}\right)\overline{\widehat{V_{b2,\iota}}\widehat{V_{b4,\iota}}} + \left(a_{13,i}a_{44,i} + a_{14,i}a_{43,i}\right)\overline{\widehat{V_{b3,\iota}}\widehat{V_{b4,\iota}}} \tag{A4}$$

$$\overline{v_\iota^{\,2}} = {a_{21,i}}^2\left(\overline{\widehat{V_{b1,\iota}}^{\,2}} + {\sigma_{13,i}}^2\right) + {a_{22,i}}^2\left(\overline{\widehat{V_{b2,\iota}}^{\,2}} + {\sigma_{24,i}}^2\right) + {a_{23,i}}^2\left(\overline{\widehat{V_{b3,\iota}}^{\,2}} + {\sigma_{13,i}}^2\right) + {a_{24,i}}^2\left(\overline{\widehat{V_{b4,\iota}}^{\,2}} + {\sigma_{24,i}}^2\right) + 2a_{21,i}a_{22,i}\overline{\widehat{V_{b1,\iota}}\widehat{V_{b2,\iota}}} + 2a_{21,i}a_{23,i}\overline{\widehat{V_{b1,\iota}}\widehat{V_{b3,\iota}}} + 2a_{21,i}a_{24,i}\overline{\widehat{V_{b1,\iota}}\widehat{V_{b4,\iota}}} + 2a_{22,i}a_{23,i}\overline{\widehat{V_{b2,\iota}}\widehat{V_{b3,\iota}}} + 2a_{22,i}a_{24,i}\overline{\widehat{V_{b2,\iota}}\widehat{V_{b4,\iota}}} + 2a_{23,i}a_{24,i}\overline{\widehat{V_{b3,\iota}}\widehat{V_{b4,\iota}}} \tag{A6}$$

$$\overline{v_\iota w_{1,\iota}} = a_{21,i}a_{31,i}\left(\overline{\widehat{V_{b1,\iota}}^{\,2}} + {\sigma_{13,i}}^2\right) + a_{22,i}a_{32,i}\left(\overline{\widehat{V_{b2,\iota}}^{\,2}} + {\sigma_{24,i}}^2\right) + a_{23,i}a_{33,i}\left(\overline{\widehat{V_{b3,\iota}}^{\,2}} + {\sigma_{13,i}}^2\right) + a_{24,i}a_{34,i}\left(\overline{\widehat{V_{b4,\iota}}^{\,2}} + {\sigma_{24,i}}^2\right) + \left(a_{21,i}a_{32,i} + a_{22,i}a_{31,i}\right)\overline{\widehat{V_{b1,\iota}}\widehat{V_{b2,\iota}}} + \left(a_{21,i}a_{33,i} + a_{23,i}a_{31,i}\right)\overline{\widehat{V_{b1,\iota}}\widehat{V_{b3,\iota}}} + \left(a_{21,i}a_{34,i} + a_{24,i}a_{31,i}\right)\overline{\widehat{V_{b1,\iota}}\widehat{V_{b4,\iota}}} + \left(a_{23,i}a_{32,i} + a_{22,i}a_{33,i}\right)\overline{\widehat{V_{b2,\iota}}\widehat{V_{b3,\iota}}} + \left(a_{22,i}a_{34,i} + a_{24,i}a_{32,i}\right)\overline{\widehat{V_{b2,\iota}}\widehat{V_{b4,\iota}}} + \left(a_{23,i}a_{34,i} + a_{24,i}a_{33,i}\right)\overline{\widehat{V_{b3,\iota}}\widehat{V_{b4,\iota}}} \tag{A7}$$

$$\overline{v_\iota w_{2,\iota}} = a_{21,i}a_{41,i}\left(\overline{\widehat{V_{b1,\iota}}^{\,2}} + {\sigma_{13,i}}^2\right) + a_{22,i}a_{42,i}\left(\overline{\widehat{V_{b2,\iota}}^{\,2}} + {\sigma_{24,i}}^2\right) + a_{23,i}a_{43,i}\left(\overline{\widehat{V_{b3,\iota}}^{\,2}} + {\sigma_{13,i}}^2\right) + a_{24,i}a_{44,i}\left(\overline{\widehat{V_{b4,\iota}}^{\,2}} + {\sigma_{24,i}}^2\right) + \left(a_{21,i}a_{42,i} + a_{22,i}a_{41,i}\right)\overline{\widehat{V_{b1,\iota}}\widehat{V_{b2,\iota}}} + \left(a_{21,i}a_{43,i} + a_{23,i}a_{41,i}\right)\overline{\widehat{V_{b1,\iota}}\widehat{V_{b3,\iota}}} + \left(a_{21,i}a_{44,i} + a_{24,i}a_{41,i}\right)\overline{\widehat{V_{b1,\iota}}\widehat{V_{b4,\iota}}} + \left(a_{23,i}a_{42,i} + a_{22,i}a_{43,i}\right)\overline{\widehat{V_{b2,\iota}}\widehat{V_{b3,\iota}}} + \left(a_{22,i}a_{44,i} + a_{24,i}a_{42,i}\right)\overline{\widehat{V_{b2,\iota}}\widehat{V_{b4,\iota}}} + \left(a_{23,i}a_{44,i} + a_{24,i}a_{43,i}\right)\overline{\widehat{V_{b3,\iota}}\widehat{V_{b4,\iota}}} \tag{A8}$$

Nomenclature

β bisector of the angle between paths of the transmitted and received pulses

γ random angle

δ angle V makes with β

ε relative root mean square error

$\Delta\phi$ phase shift

σ^2 noise if all receivers have equal noise

σ_{13}^2, σ_{24}^2 noise on longitudinal and lateral tristatic systems, respectively

τ integral time scale

a coefficient of the transformation matrix to transform between beam and Cartesian velocities

c speed of sound within the water (≈1480 m s^{-1}, dependent on temperature and salinity)

d_1, d_2 diameters of the transmitted beam at the top and bottom of a cell

D_{15}, D_{85} particle diameters for which 15% and 85% of the distribution are finer

f frequency of sound emitted by the transceiver (10 MHz)

f_s sampling frequency

i cell number

j, k, l, p indices

L cell size (= cell height)

n unbiased noise on V_b

N amplitude of incoherent backscatter

NPP number of pulse-pairs averaged by the Vectrino Profiler

ΔR_R, ΔR_T distance between a scatterer and a receiver and the transceiver, respectively

ΔR total travel distance of a pulse (= $\Delta R_T + \Delta R_R$)

Δt ping interval or time delay

Δt_D dwell time introduced when transmit pulses longer than 1 mm are combined with $\Delta t < 175$ µs

T sampling period

T transformation matrix to transform between beam and Cartesian velocities

u, v, w_1 and w_2 Cartesian velocities in the x, y, and z directions, respectively (w_1 and w_2 are independent measurements of the velocity in the z direction)

$\overline{u^2}$, $\overline{v^2}$, $\overline{w_1^2}$, $\overline{w_2^2}$ and $\overline{w_1 w_2}$ velocity variances

$\overline{uv}$, $\overline{uw_1}$, $\overline{uw_2}$, $\overline{vw_1}$ and $\overline{vw_2}$ velocity covariances

V velocity of a scatterer

V_b beam velocity; V projected onto the bisector

$\widehat{V_b}$ noise-free terms within V_b

V_{bmax} ambiguity velocity

z_1, z_2 complex-valued samples of pulses 1 and 2, respectively

ADV Acoustic Doppler velocimeter/velocimetry

ADVP Acoustic Doppler Velocity Profiler

LDV Laser Doppler velocimeter/velocimetry

R^2 complex-valued pulse-to-pulse correlation coefficient

SNR Signal-to-Noise Ratio (in dB); difference between the signal strength (in dB) and background noise (in dB)

8 References

Bendat J S, Piersol A G 1986 *Random Data: Analysis and Measurement Procedures* 2nd edn (New York, NY: John Wiley & Sons, Inc)

Benedict L H, Gould R D 1996 Towards better uncertainty estimates for turbulence statistics *Exp. Fluids* **22** 129–36

Blanckaert K, Lemmin U 2006 Means of noise reduction in acoustic turbulence measurements *J. Hydraul. Res.* **44**(1) 3–17

Brand A, Noss C, Dinkel C, Holzner M 2016 High-resolution measurements of turbulent flow close to the sediment-water interface using a bistatic acoustic profiler *J. Atmos. Ocean. Tech.* **33** 769–88

Chanson H, Trevethan M, Aoki, S 2008 Acoustic Doppler velocimetry (ADV) in small estuary: Field experience and signal post-processing *Flow Meas. Instrum.* **19** 307–13

Craig R G A, Loadman C, Clement B, Rusello P J, Siegel, E 2011 Characterization and Testing of a new Bistatic Profiling Acoustic Doppler Velocimeter: The Vectrino-II *Proceedings of the IEEE/OES/CWTM Tenth Working Conference on Current Measurement Technology (Monterey, CA)* (Piscataway, NJ: IEEE) pp 246–52

Franca M J, Lemmin U 2006 Eliminating velocity aliasing in acoustic Doppler velocity profiler data *Meas. Sci. Technol.* **17**(2) 313–22

Garcia C M, Cantero M I, Niño Y, Garcia M H 2005 Turbulence measurements with acoustic Doppler velocimeters *J. Hydraul. Eng.-ASCE* **131**(12) 1062–73

Garcia C M, Jackson P R, Garcia M H 2006 Confidence intervals in the determination of turbulence parameters *Exp. Fluids* **40** 514–22

Ghiglia D C, Pritt M D 1998 *Two-dimensional Phase Unwrapping: Theory, Algorithms, and Software* (New York, NY: John Wiley & Sons, Inc)

Holleman I, Beekhuis J 2003 Analysis and correction of dual-PRF velocity data *J. Atmos. Ocean. Tech.* **20** 443–53

Hurther D, Lemmin U 1998 A constant beamwidth transducer for 3D acoustic Doppler profile measurements in open channel flows *Meas. Sci. Technol.* **9**(10) 1706–14

Hurther D, Lemmin U 2001 A correction method for turbulence measurements with a 3D acoustic Doppler velocity profiler *J. Atmos. Ocean. Tech.* **18** 446–58

Hurther D, Thorne P D, Bricault M, Lemmin U, Barnoud J-M 2011 A multi-frequency Acoustic Concentration and Velocity Profiler (ACVP) for boundary layer

measurements of fine-scale flow and sediment transport processes *Coast. Eng.* 58(7) 594–605

Joe P, May P T 2003 Correction of dual PRF velocity errors for operational Doppler weather radars *J. Atmos. Ocean. Tech.* **20** 429–42

Kalantari L S, Mohanna S, Tavakoli S 2009 Detection, identification and tracking of flying objects in three dimensions using multistatic radars *International Journal of Communications, Network and System Sciences* **6** 486–90

Kraus N C, Lohrmann A, Cabrera R 1994 New acoustic meter for measuring 3D laboratory flows *J. Hydraul. Eng.-ASCE* **120**(3) 406–12

Lemmin U, Rolland T 1997 Acoustic velocity profiler for laboratory and field studies *J. Hydraul. Eng.-ASCE* **123**(12) 1089–98

Leng X, Chanson H 2017 Unsteady velocity profiling in bores and positive surges. *Flow Meas. Instrum.* **54** 136–145

Lhermitte R, Lemmin U 1994 Open-channel flow and turbulence measurement by high-resolution Doppler sonar *J. Atmos. Ocean. Tech.* **11**(5) 1295–1308

Lhermitte R, Serafin R 1984 Pulse-to-pulse coherent Doppler sonar signal processing techniques *J. Atmos. Ocean. Tech.* **1**(4) 293–308

Lohrmann A, Cabrera R, Gelfenbaum G, Haines J 1995 Direct measurements of Reynolds stress with an acoustic Doppler velocimeter *Proceedings of the IEEE Fifth Working Conference on Current Measurements* (St. Petersburg, FL: IEEE Oceanic Engineering Society) pp 205–10

McLelland S J, Nicholas A P 2000 A new method for evaluating errors in high-frequency ADV measurements *Hydrol. Process.* **14** 351–66

MacVicar B, Dilling S, Lacey J, Hipel K 2014 A quality analysis of the Vectrino II instrument using a new open-source MATLAB toolbox and 2D ARMA models to detect and replace spikes *Proc. Riverflow 2014–Int. Conf. Fluvial Hydraulics* (Balkema, Leiden: CRC Press) pp 1951–59

Miller K S, Rochwarger M M 1972 A covariance approach to spectral moment estimation *IEEE T. Inform. Theory.* **IT-18** 588–96

Nortek 1997 *ADV Operation Manual* (Vollen, Norway: Nortek AS)

Nortek 2012 *Amplitude and correlation calculations for Vectrino II* (posted by Jonas Røstad, November 28, 2012) http://www.nortek-as.com/en/knowledge-center/forum/vectrinoii/864427573 Accessed 26 February 2016

Nortek 2015a *MIDAS Data Acquisition Software; Software User Guide* (Boston, MA: Nortek Scientific Acoustic Development Group Inc)

Nortek 2015b *Comprehensive Manual* (Rud, Norway: Nortek AS)

NortekUSA 2013 Tutorial -> Vectrino II -> Configuration (March 26, 2013) http://www.nortekusa.com/usa/knowledge-center/table-of-contents/vectrino-ii/configuration Accessed 31 October 2016

Parkhurst J M, Price G J, Sharrock P J, Moore C J 2011 Phase unwrapping algorithms for use in a true real-time optical body sensor system for use during radiotherapy *Appl. Optics* **50**(35) 6430–39

Poindexter C M, Rusello P J, Variano E A 2011 Acoustic Doppler velocimeter-induced acoustic streaming and its implications for measurement *Exp. Fluids* **50** 1429–42

SonTek 1997 *Acoustic Doppler Velocimeter (ADV) principles of operation* (San Diego, CA: SonTek)

SonTek/YSI 2001 *ADVField operation manual* (San Diego, CA: SonTek/YSI)

SonTek/YSI 2016 Sontek-SL series http://www.sontek.com/productsdetail.php?SonTek-SL-8 Accessed 8 November 2016

Soulsby R L 1980 Selecting record length and digitization rate for near-bed turbulence measurements *J. Phys. Oceanogr.* **10**(2) 208–19

Strom K B, Papanicolaou A N 2007 ADV Measurements around a cluster microform in a shallow mountain stream *J. Hydraul. Eng.-ASCE* **133**(12) 1379–89

Tennekes H, Lumley J L 1972 *A First Course in Turbulence* (Cambridge, MA: MIT Press)

Ursic M, Langendoen E J, Wren D G, Kuhnle R A, Pellachini C 2012 Performance assessment and calibration of a profiling lab-scale acoustic Doppler velocimeter for application over mixed sand-gravel beds *Proceedings of the ASCE/EWRI Hydraulic Measurements and Experimental Methods Conference (Snowbird, UT, 12-15 August 2012)* (Reston, VA: ASCE)

Voulgaris G, Trowbridge J H 1998 Evaluation of the acoustic Doppler velocimeter (ADV) for turbulence measurements *J. Atmos. Ocean. Tech.* **15** 272–89

Wahl T L 2003 Discussion of "Despiking acoustic Doppler velocimeter data" by Derek G. Goring and Vladimir I. Nikora *J. Hydraul. Eng.-ASCE* **129**(6) 484–87

Zappa E, Busca G 2008 Comparison of eight unwrapping algorithms applied to Fourier-transform profilometry *Opt. Laser Eng.* **46**(2) 106–16

Zedel L 2008 Modeling pulse-to-pulse coherent Doppler Sonar *J. Atmos. Ocean. Tech.* **25**(10) 1834–44

Zedel L 2015 Modelling Doppler sonar backscatter *Proceedings of the 2015 IEEE/OES Eleventh Current, Waves and Turbulence Measurement Workshop (St. Petersburg, FL, 2-6 March 2015)* (doi: 10.1109/CWTM.2015.7098132)

Zedel L, Hay A E 2002 A three-component bistatic coherent Doppler velocity profiler: Error sensitivity and system accuracy *IEEE J. Oceanic Eng.* **27**(3) 717–25

Zedel L, Hay A E 2011 Turbulence measurements in a jet: Comparing the Vectrino and VectrinoII *Proceedings of the IEEE/OES/CWTM Tenth Working Conference on Current Measurement Technology (Monterey, CA)* (Piscataway, NJ: IEEE) pp 246–52

Zedel L, Hay A E, Cabrera R, Lohrmann A 1996 Performance of a single-beam pulse-to-pulse coherent Doppler profiler *IEEE J. Oceanic Eng.* **21**(3) 290–97

Zrnic D S 1977 Spectral moment estimates from correlated pulse pairs *IEEE T. Aero. Elec. Sys.* **AES-9** 151–65

Figures

Figure 1. (a) Illustration of the operation principle of the Vectrino Profiler profiling ADV, showing the cause of the phase difference detected between the emission of Pulses 1 and 2. Note that the geometry of the acoustic pulse paths is exaggerated to aid visualisation; (b) Definition of the parameters of equations (4) and (5), where R_T is the distance between a scatterer and the transceiver, R_R is the distance between a scatterer and a receiver, **V** is the velocity vector of a scatterer, which makes a random angle δ with the bisector of the angle β between the paths of the transmitted and received pulses. The red collar signifies the receiver arm that points in the positive *x*-direction.

Figure 2. Schematic illustration of the signal strength received by the receivers of a Vectrino Profiler profiling ADV and range gating. The horizontal axis denotes time, but has been written as distance from the central transceiver.

Figure 3. a) Schematic illustration of the location of the sampling volumes of the Vectrino Profiler (not to scale). The red collar signifies the receiver arm that points in the positive *x*-direction. Note that the Vectrino Profiler has a right-handed coordinate system. b) The methodology used in Experiment 2: after a measurement, the Vectrino Profiler was moved vertically by one 2 mm cell height, so that in the subsequent measurement, the same physical location was located in the neighbouring cell above. A similar methodology was adopted in Experiment 3, except that the Vectrino Profiler was moved vertically by an increment of four 1 mm cell heights.

Figure 4. Range below transmitter against mean amplitude for 1 mm cells for an example Vectrino Profiler (Experiment 1).

Figure 5. Range below transmitter against mean amplitude for 4 mm cells for an example Vectrino Profiler (Experiment 1).

Figure 6. Range below transmitter against mean correlation for 1 mm cells for an example Vectrino Profiler (Experiment 1).

Figure 7. Range below transmitter against mean correlation for 4 mm cells for an example Vectrino Profiler (Experiment 1).

Figure 8. Variation of parameters at a height of 30 mm above the bed, quantified by raising the Vectrino Profiler in increments of one cell height (cell height = 2 mm) between each 120 s sampling period (Experiment 2). Cell number 6 contains the sweet spot. All Kaolin series were measured with the high power setting. (a) mean longitudinal velocity (error bars represent 95% confidence intervals); (b) Noise on receivers 1 and 3; (c) mean SNR in the plane of receivers 1 and 3; and (d) Noise on receivers 2 and 4. Note that results obtained when the probe was oriented at 90° and 180° have been transformed so that they have the same direction as the measurement undertaken at an orientation of 0°. Thus, the longitudinal tristatic system at an orientation of 90° is the lateral tristatic system at an orientation of 0° and the lateral tristatic system at an orientation of 90° is the longitudinal tristatic system at an orientation of 0°.

Figure 9. Variation of parameters at a height of 30 mm above the bed, quantified by raising the Vectrino Profiler in increments of four cell heights (cell height = 1 mm) between each 240 s sampling period (Experiment 3). The sweet spot occurs between positions 3 and 4. Black lines and circles: pump frequency 10 Hz, ambiguity velocity 0.085 m s^{-1}; mid-grey lines and triangles: pump frequency 10 Hz, ambiguity velocity 0.185 m s^{-1}; light-grey lines and diamonds: pump frequency 10 Hz, ambiguity velocity 0.343 m s^{-1}. (a) mean longitudinal velocity (error bars represent 95% confidence intervals); (b) Noise on receivers 1 and 3 normalised by the (virtually noise free) vertical normal stress; (c) mean SNR in the plane of receivers 1 and 3; and (d) Noise on receivers 2 and 4 normalised by the (virtually noise free) vertical normal stress.

Figure 10. Variation of parameters at a height of 30 mm above the bed, quantified by raising the Vectrino Profiler in increments of four cell heights (cell height = 1 mm) between each 240 s sampling period (Experiment 3). The sweet spot occurs between positions 3 and 4. Black lines and circles: pump frequency 25 Hz, ambiguity velocity 0.185 m s^{-1}; grey lines and triangles: pump frequency 25 Hz, ambiguity velocity 0.343 m s^{-1}. (a) mean longitudinal velocity (error bars represent 95% confidence intervals); (b) Noise on receivers 1 and 3 normalised

by the (virtually noise free) vertical normal stress; (c) mean SNR in the plane of receivers 1 and 3; and (d) Noise on receivers 2 and 4 normalised by the (virtually noise free) vertical normal stress.

Figure 11. Variation of mean beam velocities (error bars represent 95% confidence intervals) at a height of 30 mm above the bed, quantified by raising the Vectrino Profiler in increments of four cell heights (cell height = 1 mm) between each 240 s sampling period (Experiment 3). The sweet spot occurs between positions 3 and 4. (a) pump frequency 10 Hz, (b) pump frequency 25 Hz. Black lines: ambiguity velocity 0.085 m s^{-1}; blue lines: ambiguity velocity 0.185 m s^{-1}; red lines: ambiguity velocity 0.343 m s^{-1}.

Figure 12. Variation of noise parameters at a height of 30 mm above the bed, quantified by raising the Vectrino Profiler in increments of one cell height (cell height = 2 mm) between each 120 s sampling period (Experiment 2, clear water, high power series). Cell number 6 contains the sweet spot. (a) noise according to the correction method of Hurther and Lemmin (2001) and the correction method presented herein; (b) percentage difference between vertical velocity variances; (c) longitudinal velocity variance; and (d) lateral velocity variance.

Figure 13. Comparison of theoretical (equation 13C) and empirical transformation matrix coefficients, a_{ij} (equation 13B), of the Vectrino Profiler with probe and hardware serial numbers VCN8773 and VNO1468, respectively, prior to and after recalibration by Nortek. (a) positive coefficients that dominate the transformation from beam velocities to u and v, a_{11} and a_{22}, respectively; (b) negative coefficients that dominate the transformation from beam velocities to u and v, a_{13} and a_{24}, respectively; (c) cross-tristatic system coefficients; (d) coefficients that dominate the transformation from beam velocities to w_1 and w_2, a_{31} and a_{33}, and a_{42} and a_{44}, respectively.

Figure 14. Estimated measurement volumes (colour bands) of the Vectrino Profiler for a cell height of 2 mm. The acoustic beams are also drawn, showing the assumed width and spreading angle of the beams. Open circles present the centres of the measurement volumes, while the crosses present those of the other receiver located in the same plane.

Table 1. Noise multiplier magnitudes for variances and covariances measured with the Vectrino Profiler with probe and hardware serial numbers VCN8773 and VNO1468, respectively, prior to recalibration by Nortek.

Cell number	$\overline{u^2}$ $\sum_{j=1}^{j=4} {a_{1j}}^2$	$\overline{uv}$ $\sum_{j=1}^{j=4} a_{1j}a_{2j}$	$\overline{uw_1}$ $\sum_{j=1}^{j=4} a_{1j}a_{3j}$	$\overline{uw_2}$ $\sum_{j=1}^{j=4} a_{1j}a_{4j}$	$\overline{v^2}$ $\sum_{j=1}^{j=4} {a_{2j}}^2$	$\overline{vw_1}$ $\sum_{j=1}^{j=4} a_{2j}a_{3j}$	$\overline{vw_2}$ $\sum_{j=1}^{j=4} a_{2j}a_{4j}$	$\overline{{w_1}^2}$ $\sum_{j=1}^{j=4} {a_{3j}}^2$	$\overline{w_1w_2}$ $\sum_{j=1}^{j=4} a_{3j}a_{4j}$	$\overline{{w_2}^2}$ $\sum_{j=1}^{j=4} {a_{4j}}^2$
1	8.445	0.243	0.148	0.128	8.193	0.144	0.123	0.537	0.004	0.537
2	8.389	0.265	0.142	0.124	8.138	0.147	0.127	0.537	0.004	0.537
3	8.304	0.284	0.138	0.118	8.084	0.148	0.131	0.538	0.005	0.537
4	8.241	0.297	0.138	0.113	8.043	0.149	0.134	0.538	0.005	0.538
5	8.163	0.301	0.135	0.107	8.015	0.151	0.139	0.538	0.005	0.538
6	8.131	0.305	0.132	0.107	7.971	0.150	0.139	0.539	0.005	0.538
7	8.086	0.307	0.129	0.104	7.956	0.151	0.143	0.538	0.005	0.538
8	8.050	0.298	0.125	0.101	7.903	0.148	0.142	0.538	0.004	0.538
9	7.995	0.286	0.121	0.098	7.863	0.148	0.143	0.539	0.004	0.538
10	7.917	0.281	0.116	0.096	7.817	0.145	0.138	0.539	0.004	0.538
11	7.911	0.262	0.114	0.097	7.789	0.148	0.131	0.539	0.004	0.538
12	7.939	0.244	0.117	0.098	7.780	0.145	0.135	0.539	0.004	0.538
13	7.886	0.238	0.117	0.097	7.731	0.145	0.139	0.539	0.004	0.539
14	7.815	0.223	0.113	0.096	7.658	0.146	0.138	0.539	0.004	0.539
15	7.783	0.210	0.114	0.096	7.619	0.146	0.137	0.539	0.004	0.539
16	7.760	0.199	0.116	0.096	7.592	0.147	0.137	0.540	0.004	0.539
17	7.670	0.210	0.115	0.094	7.562	0.147	0.135	0.540	0.004	0.539
18	7.602	0.203	0.112	0.096	7.507	0.148	0.134	0.540	0.004	0.540
19	7.556	0.206	0.112	0.097	7.468	0.147	0.134	0.541	0.004	0.540
20	7.496	0.209	0.111	0.097	7.409	0.148	0.129	0.541	0.004	0.540
21	7.440	0.214	0.112	0.099	7.327	0.146	0.127	0.541	0.004	0.540
22	7.366	0.236	0.113	0.097	7.272	0.148	0.123	0.542	0.004	0.541
23	7.349	0.241	0.115	0.094	7.210	0.146	0.114	0.542	0.004	0.540
24	7.277	0.262	0.117	0.094	7.156	0.145	0.104	0.542	0.004	0.541
25	7.216	0.272	0.113	0.091	7.120	0.142	0.100	0.542	0.004	0.541
26	7.139	0.266	0.113	0.090	7.072	0.137	0.103	0.543	0.004	0.541
27	7.031	0.265	0.108	0.088	7.051	0.134	0.102	0.543	0.003	0.541
28	6.934	0.264	0.106	0.084	7.033	0.133	0.099	0.543	0.003	0.541
29	6.846	0.233	0.103	0.082	7.032	0.137	0.101	0.544	0.003	0.541
30	6.701	0.228	0.094	0.078	7.023	0.143	0.107	0.545	0.003	0.541
31	6.572	0.214	0.088	0.073	7.049	0.152	0.115	0.546	0.003	0.541
32	6.442	0.200	0.081	0.070	7.042	0.158	0.119	0.547	0.004	0.541
33	6.337	0.194	0.076	0.069	7.036	0.164	0.114	0.548	0.004	0.541
34	6.233	0.218	0.072	0.067	7.050	0.166	0.110	0.549	0.004	0.541
35	6.180	0.221	0.067	0.070	7.081	0.164	0.100	0.549	0.003	0.540

Table 2. Estimated location of the centres of the measurement volumes and the lateral mismatch between the two receivers located in the same plane.

Cell number	Vertical distance (mm)	Lateral distance (mm)	Lateral mismatch between two co-planar receivers (mm)
1	40.1	2.2	4.4
2	41.1	1.9	3.8
3	42.1	1.6	3.3
4	43.1	1.4	2.7
5	44.1	1.1	2.2
6	45.1	0.8	1.7
7	46.1	0.6	1.1
8	47.1	0.3	0.6
9	48.1	0.1	0.2
10	49.1	-0.1	-0.1
11	50.1	-0.3	-0.7
12	51.1	-0.6	-1.2
13	52.1	-0.9	-1.7
14	53.1	-1.1	-2.3
15	54.1	-1.4	-2.8
16	55.1	-1.7	-3.3
17	56.1	-1.9	-3.9
18	57.1	-2.2	-4.4
19	58.1	-2.5	-4.9
20	59.1	-2.7	-5.5
21	60.1	-3.0	-6.0
22	61.1	-3.3	-6.5
23	62.1	-3.5	-7.1
24	63.1	-3.8	-7.6
25	64.1	-4.1	-8.2
26	65.1	-4.3	-8.7
27	66.1	-4.6	-9.2
28	67.1	-4.9	-9.7
29	68.1	-5.1	-10.3
30	69.1	-5.4	-10.8
31	70.1	-5.7	-11.3
32	71.1	-5.9	-11.9
33	72.0	-6.2	-12.4
34	73.0	-6.5	-12.9
35	73.9	-6.7	-13.4

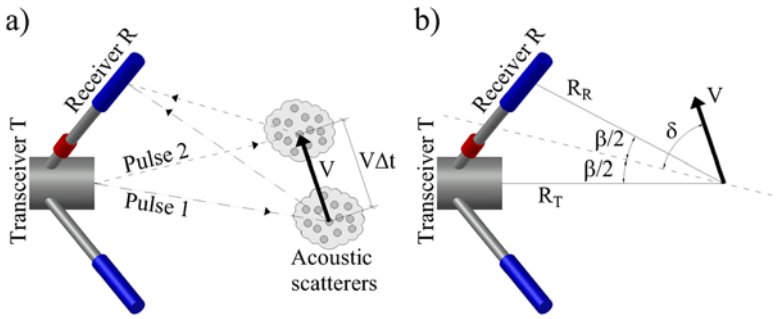

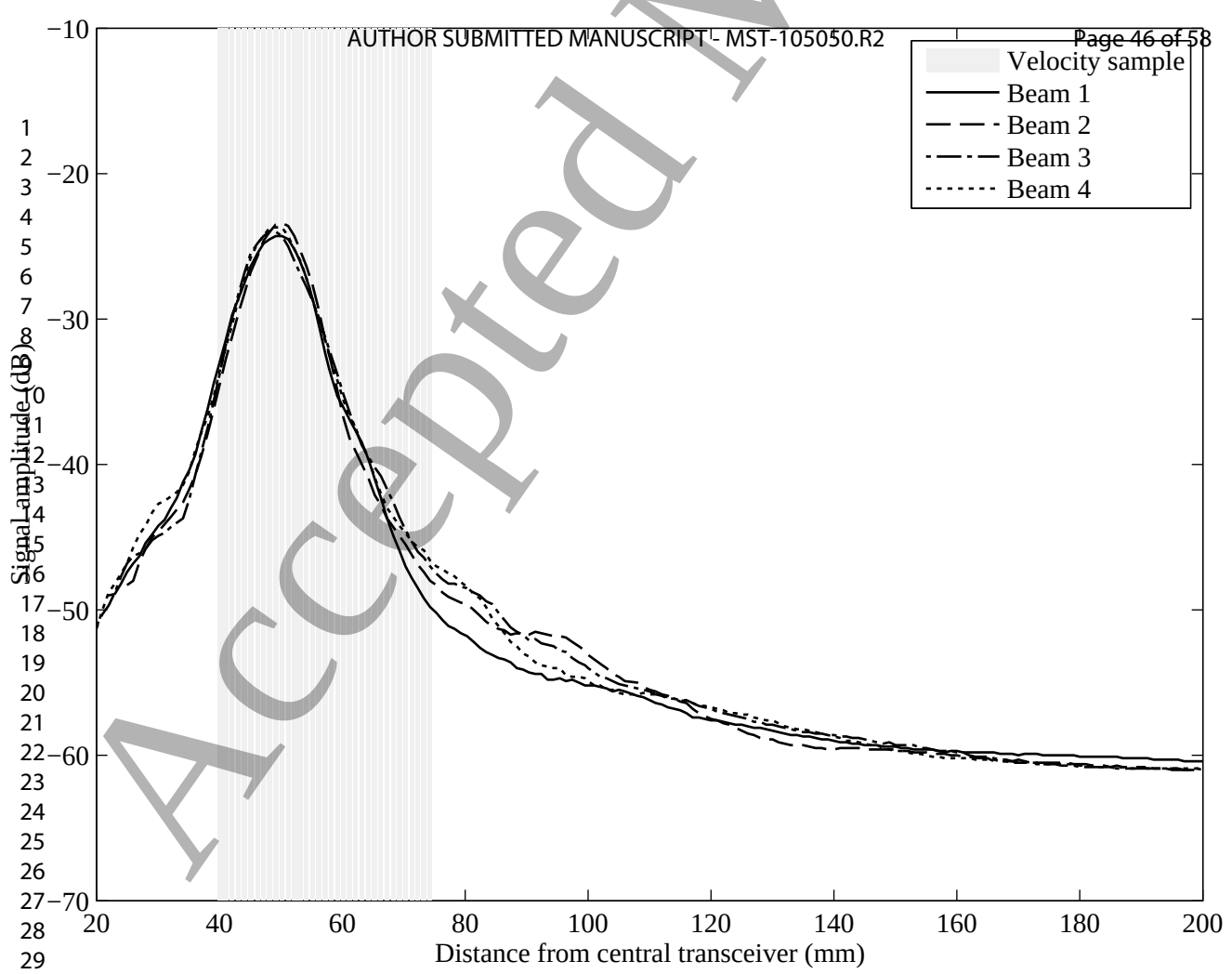
Velocity sample
Beam 1
Beam 2
Beam 3
Beam 4
Signal amplitude (dB)
−10
−20
−30
−40
−50
−60
−70
20
40
60
80
100
120
140
160
180
200
Distance from central transceiver (mm)

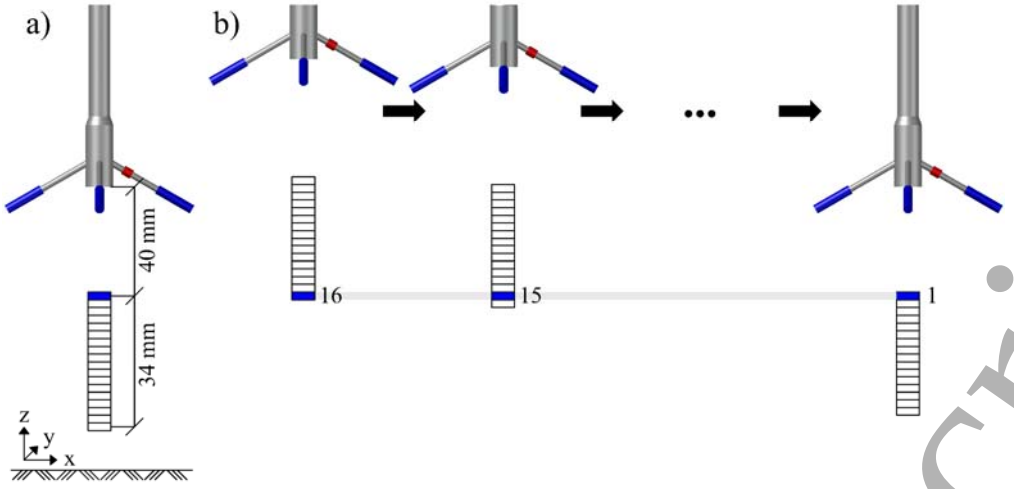

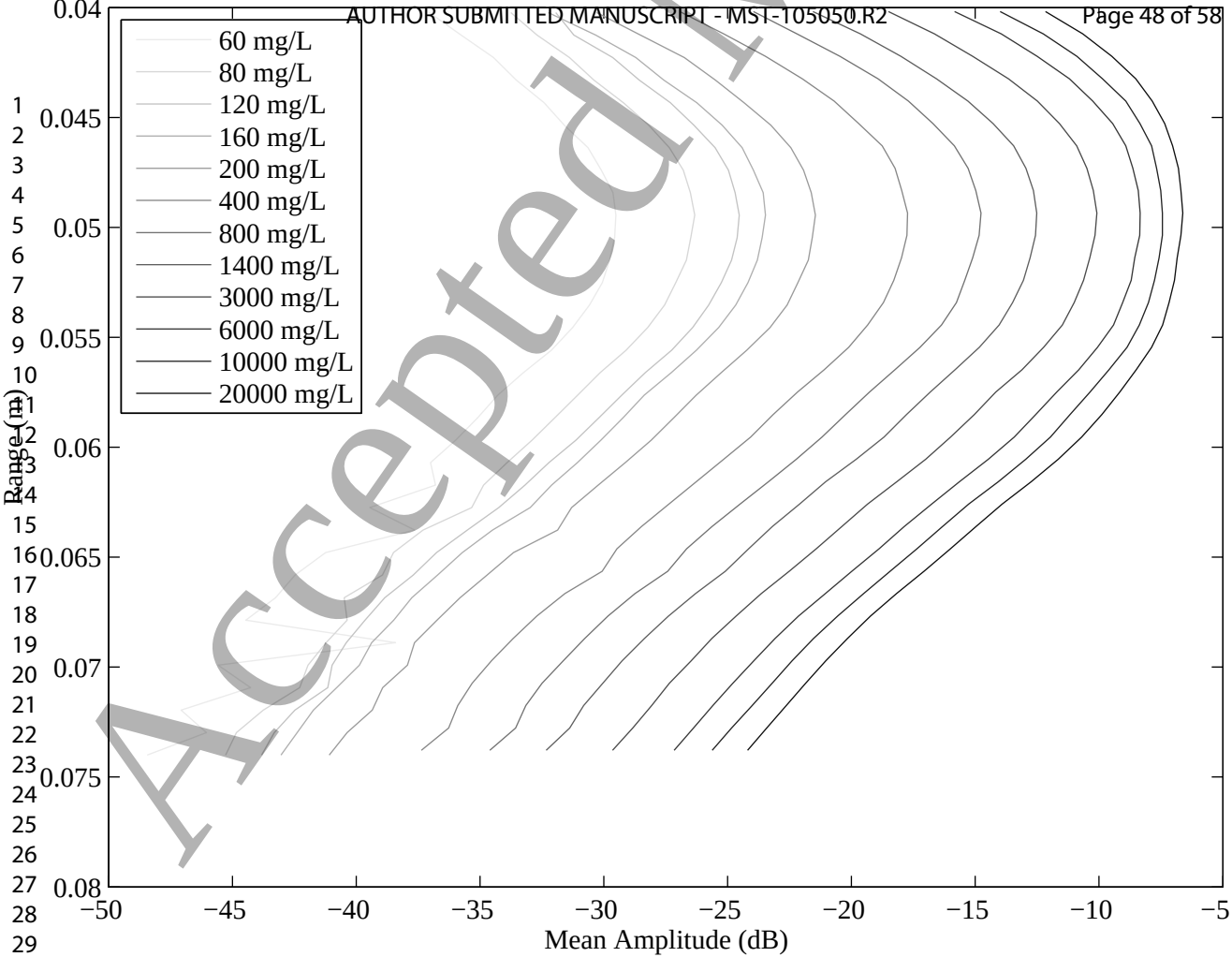
60 mg/L
80 mg/L
120 mg/L
160 mg/L
200 mg/L
400 mg/L
800 mg/L
1400 mg/L
3000 mg/L
6000 mg/L
10000 mg/L
20000 mg/L
Range (m)
0.04
0.045
0.05
0.055
0.06
0.065
0.07
0.075
0.08
−50
−45
−40
−35
−30
−25
−20
−15
−10
−5
Mean Amplitude (dB)

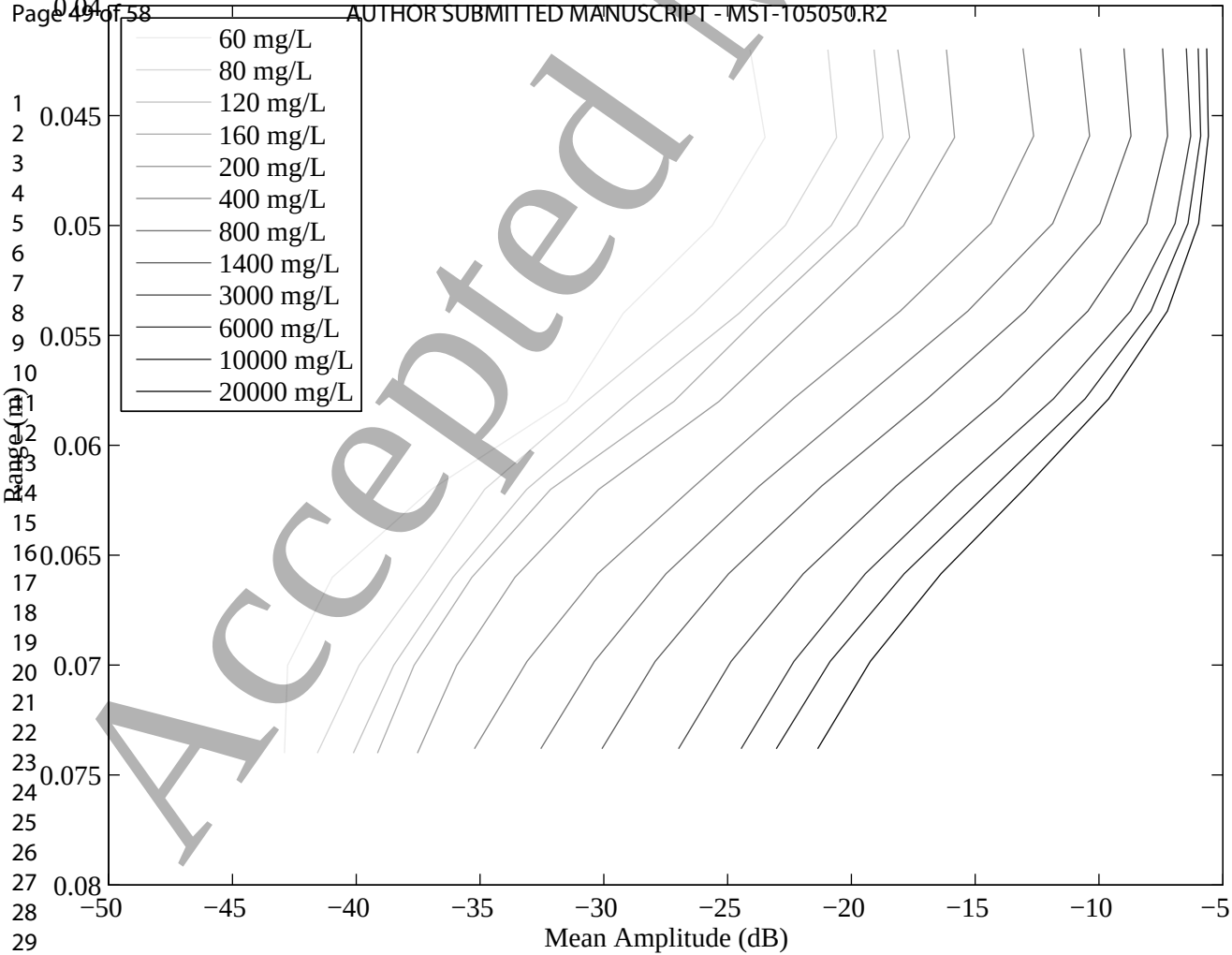
60 mg/L
80 mg/L
120 mg/L
160 mg/L
200 mg/L
400 mg/L
800 mg/L
1400 mg/L
3000 mg/L
6000 mg/L
10000 mg/L
20000 mg/L
Range (m)
0.04
0.045
0.05
0.055
0.06
0.065
0.07
0.075
0.08
−50
−45
−40
−35
−30
−25
−20
−15
−10
−5
Mean Amplitude (dB)

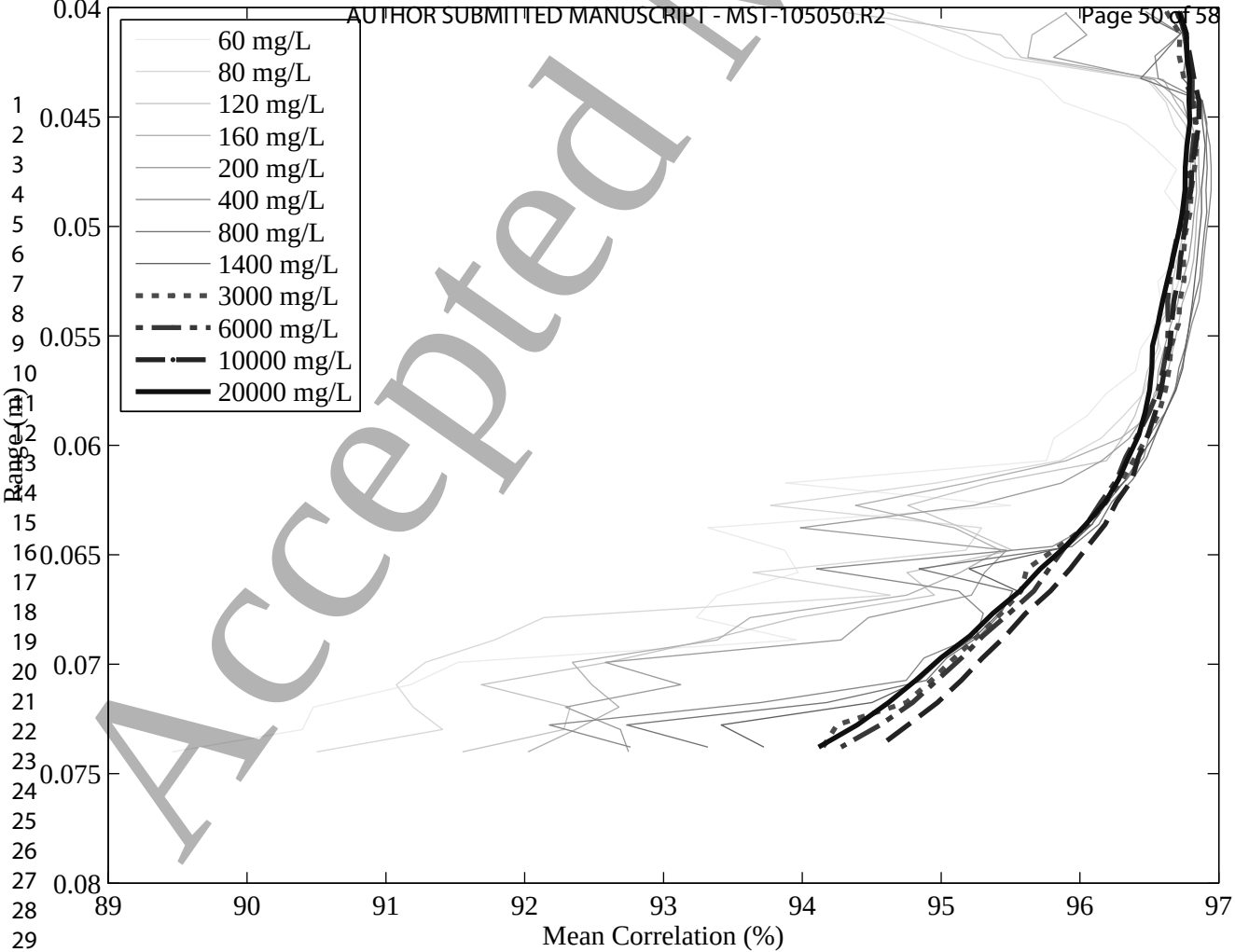
60 mg/L
80 mg/L
120 mg/L
160 mg/L
200 mg/L
400 mg/L
800 mg/L
1400 mg/L
3000 mg/L
6000 mg/L
10000 mg/L
20000 mg/L
Range (m)
0.04
0.045
0.05
0.055
0.06
0.065
0.07
0.075
0.08
89
90
91
92
93
94
95
96
97
Mean Correlation (%)

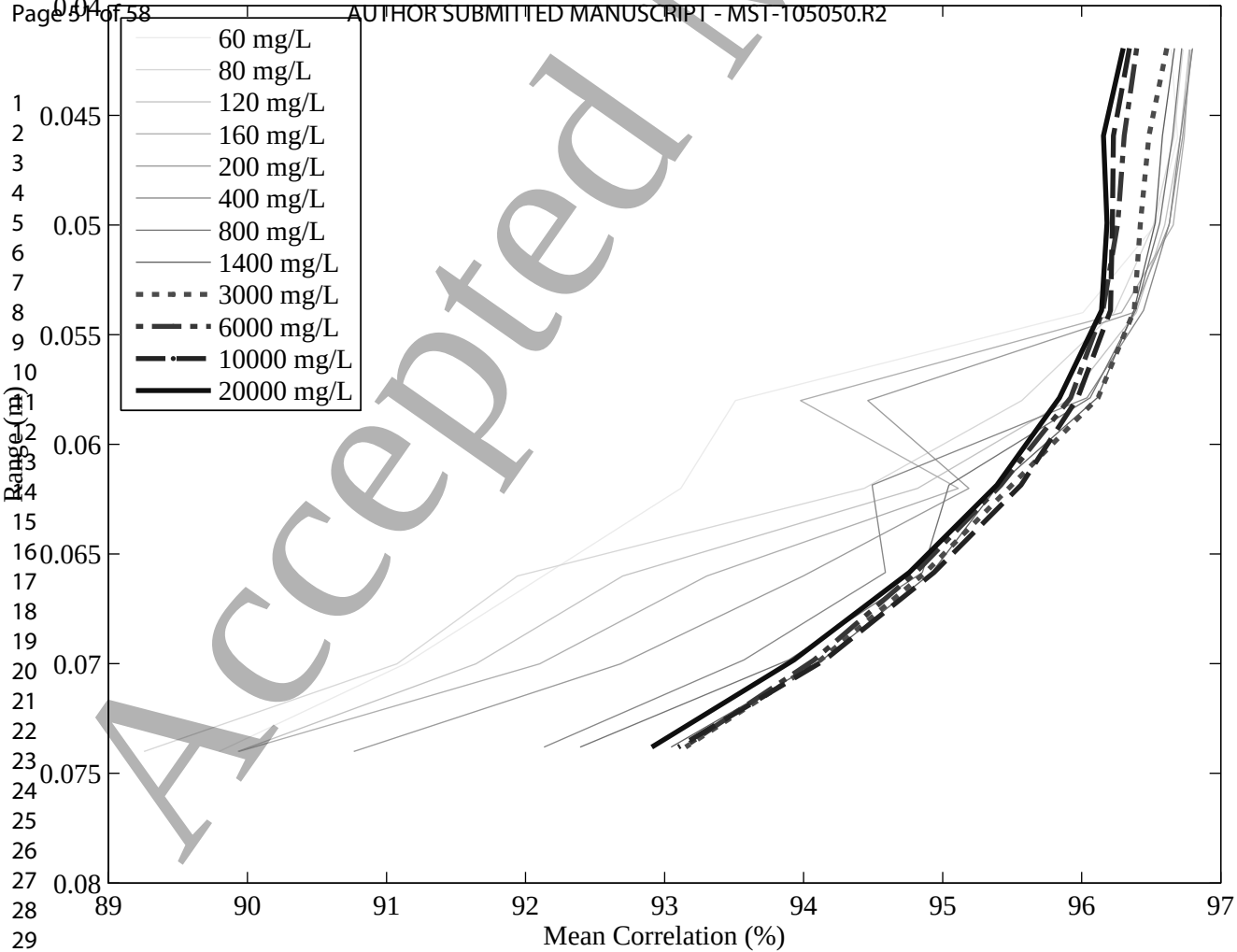
60 mg/L
80 mg/L
120 mg/L
160 mg/L
200 mg/L
400 mg/L
800 mg/L
1400 mg/L
3000 mg/L
6000 mg/L
10000 mg/L
20000 mg/L
Range (m)
0.04
0.045
0.05
0.055
0.06
0.065
0.07
0.075
0.08
89
90
91
92
93
94
95
96
97
Mean Correlation (%)

(a)

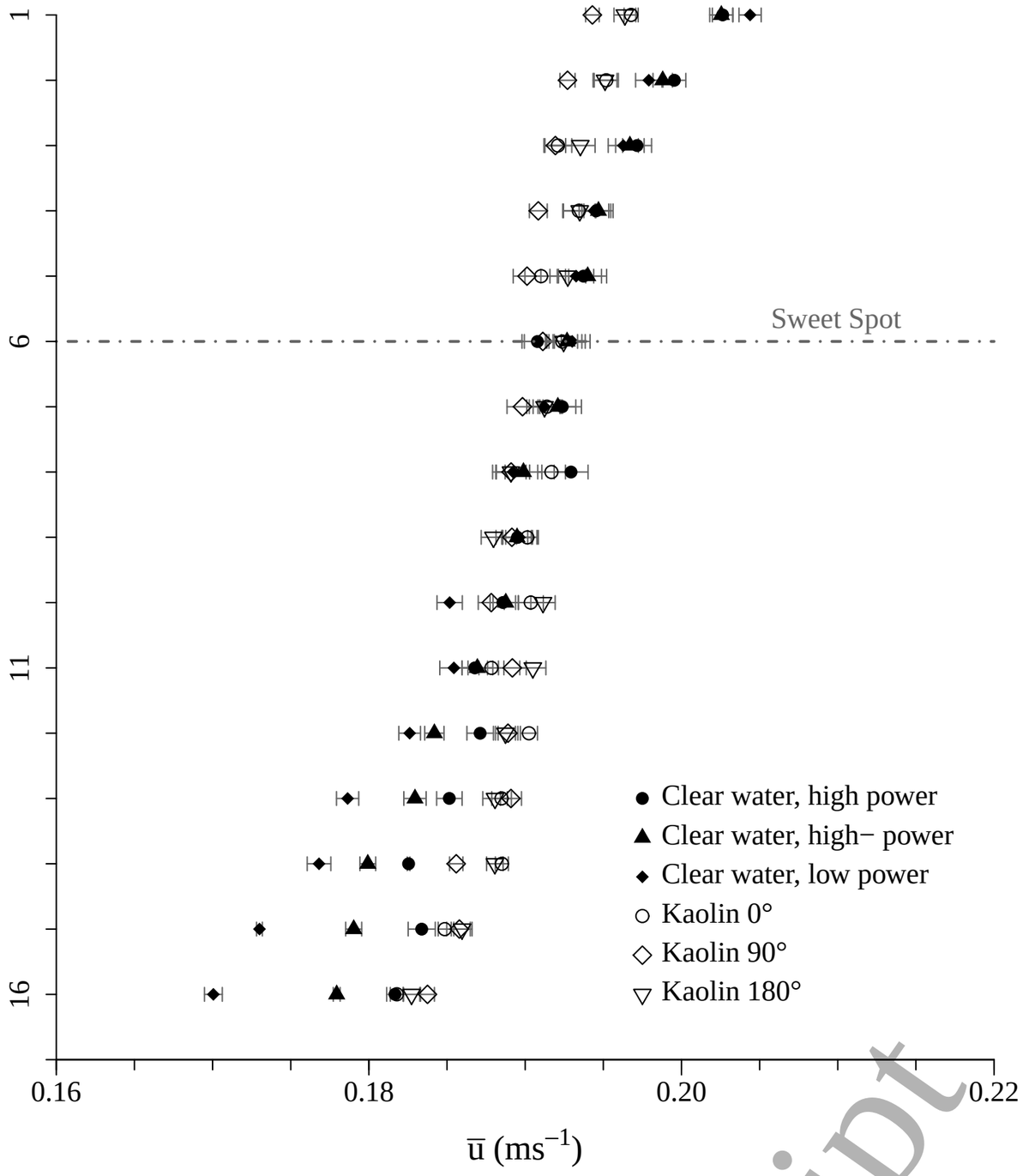

(b)

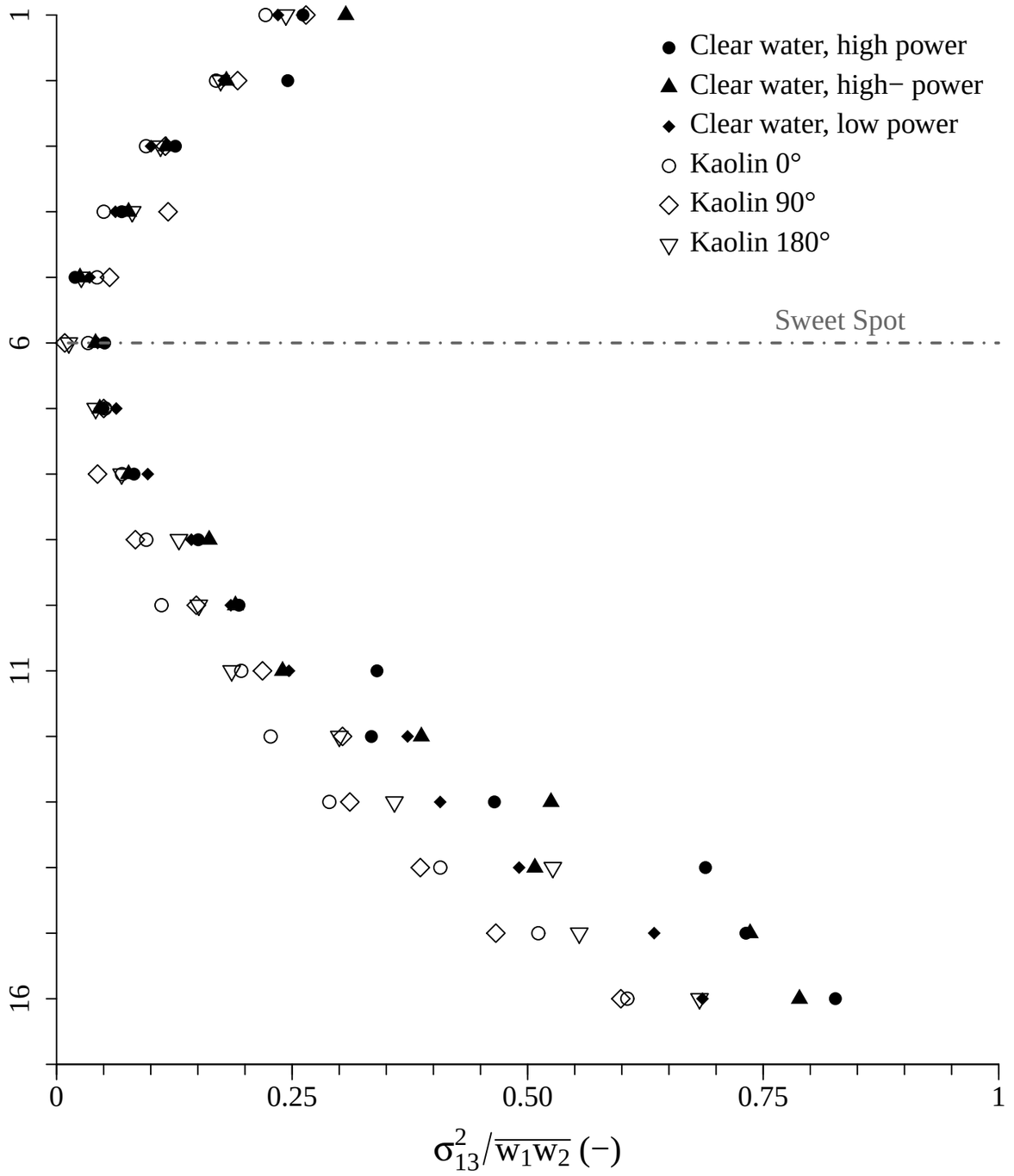

(c)

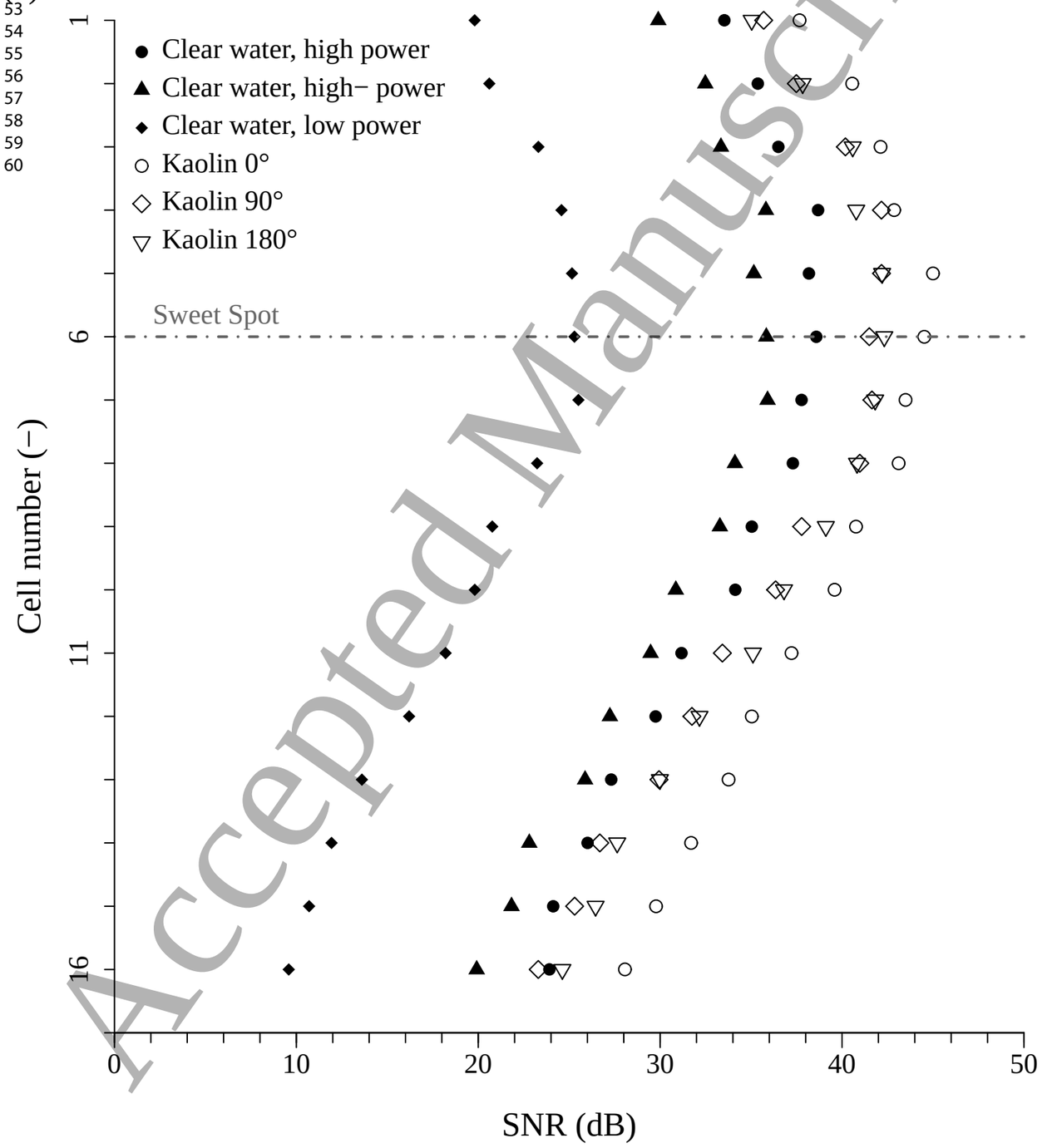

(d)

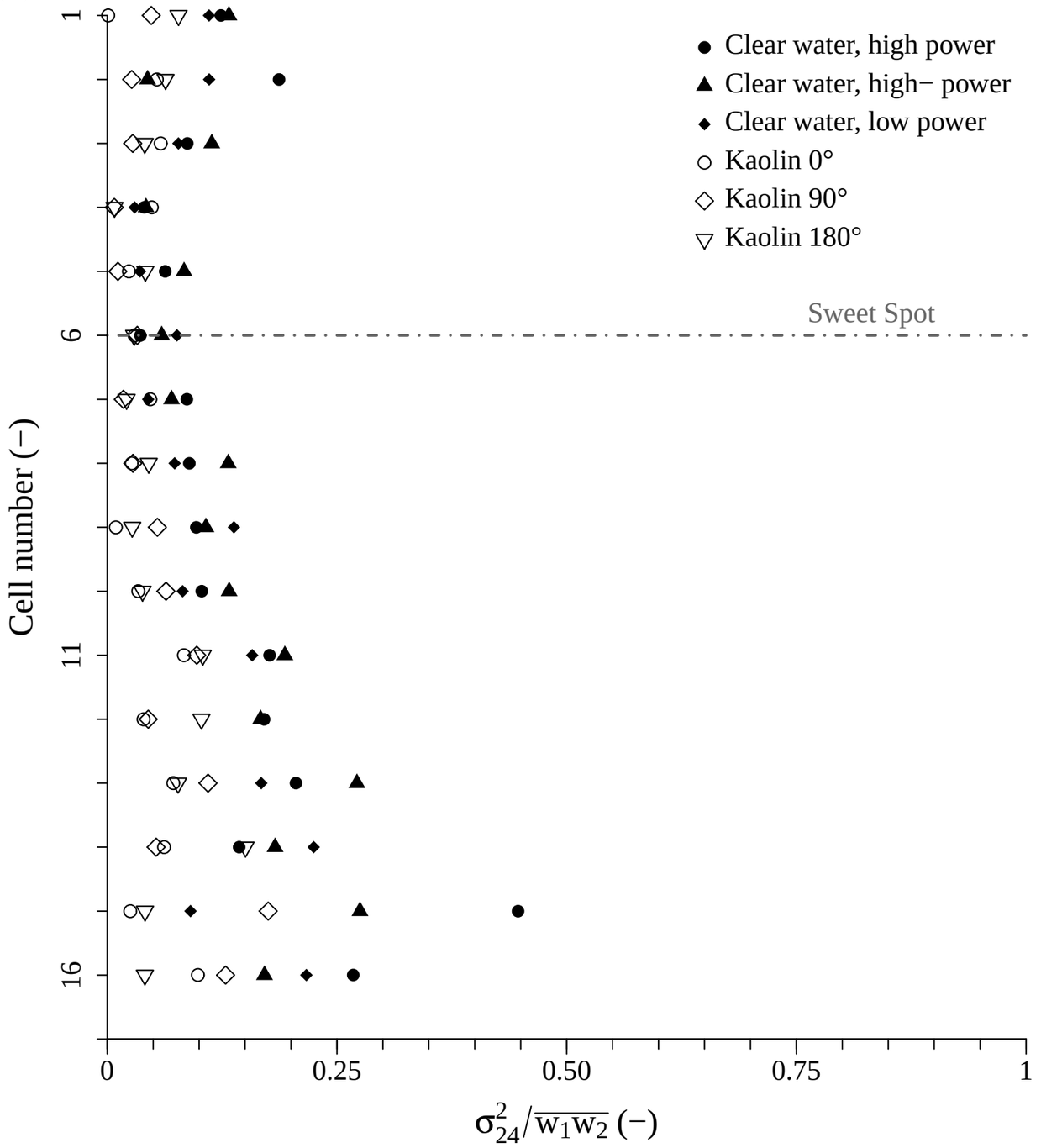

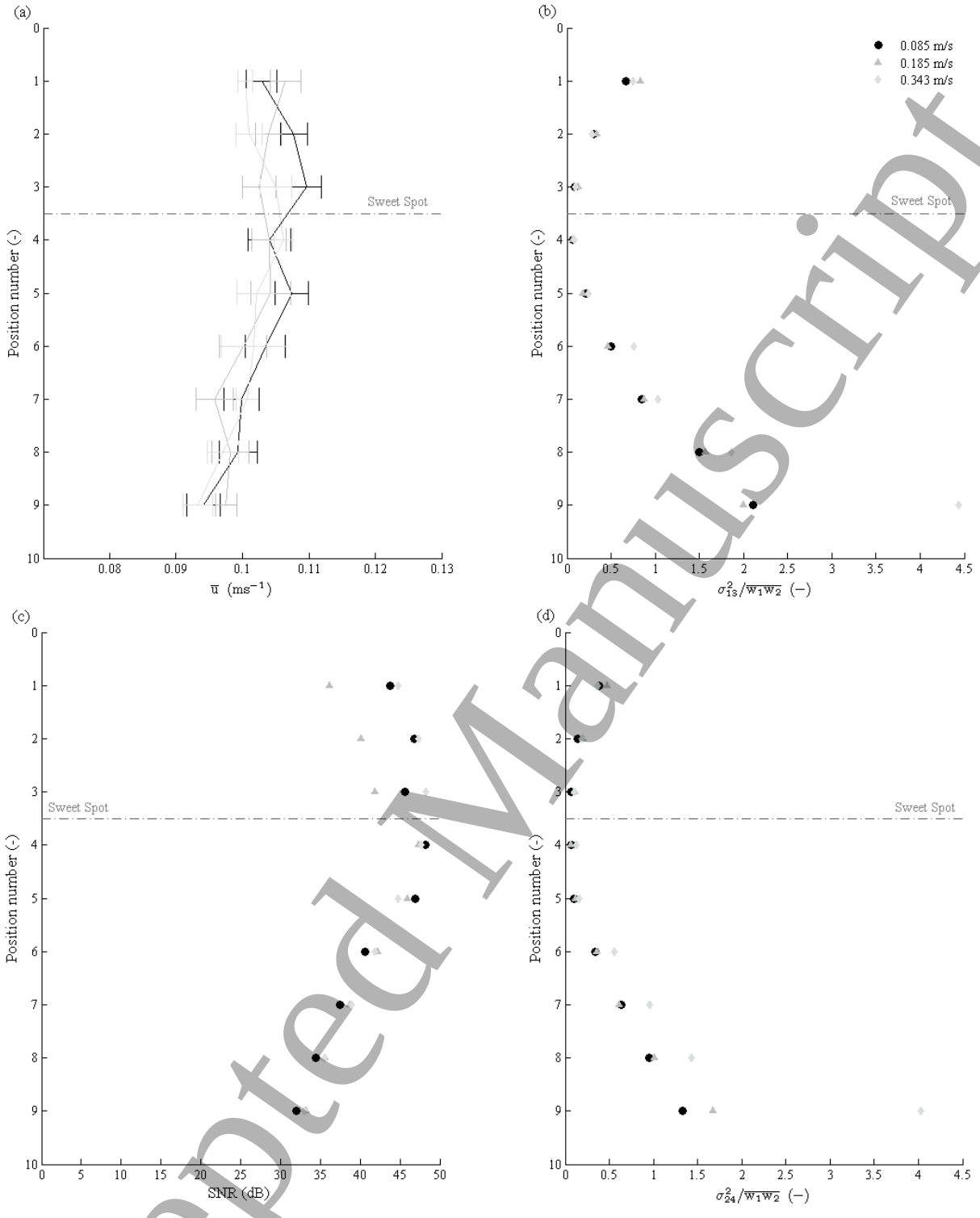

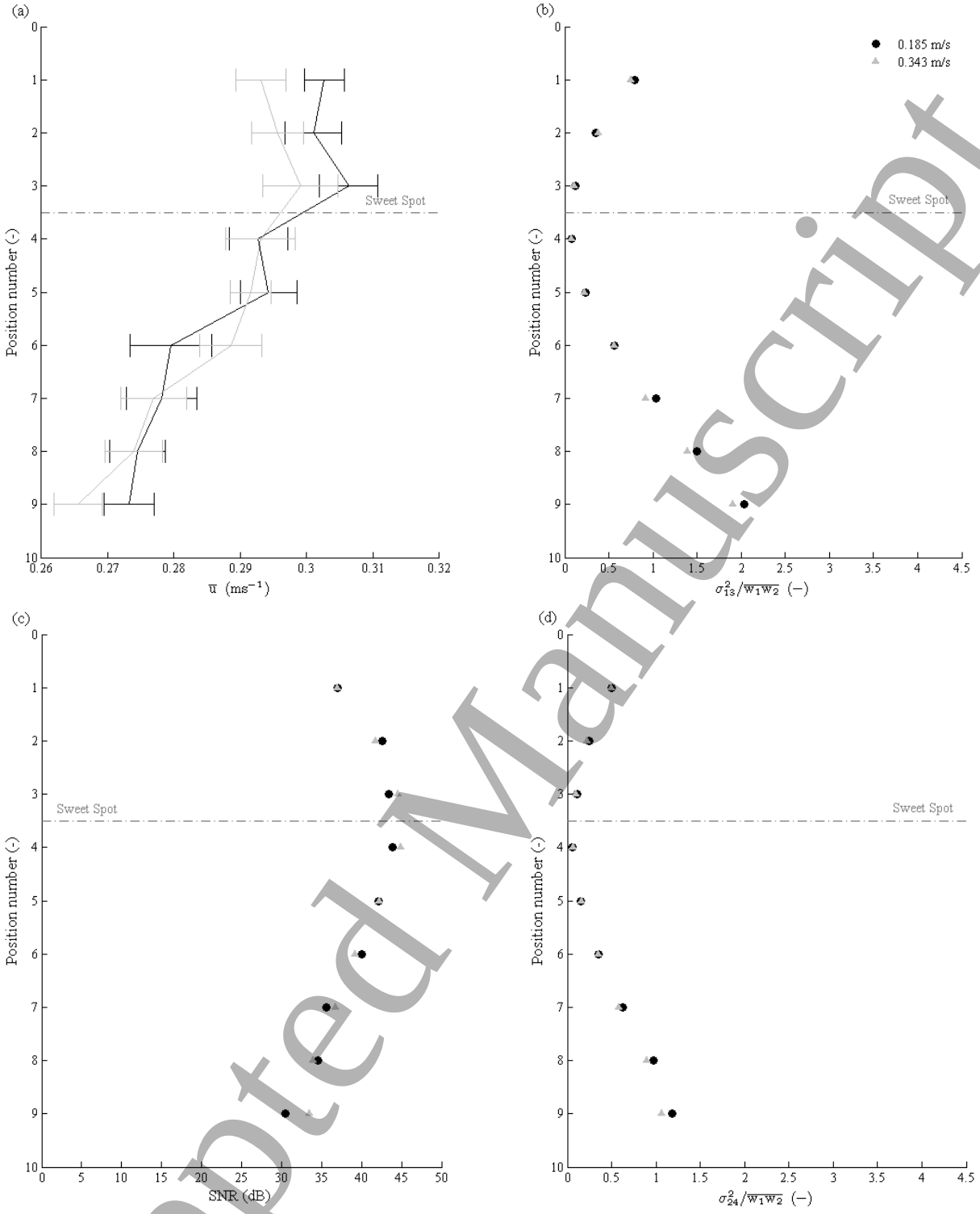

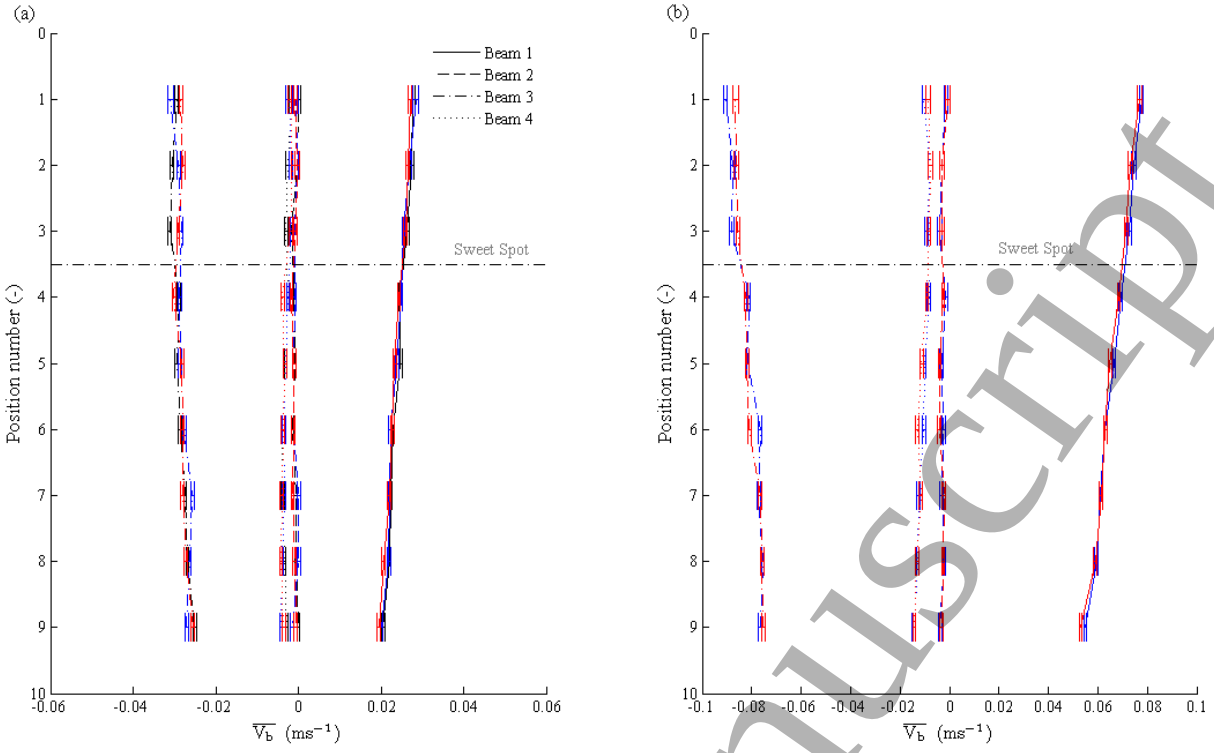

(a)

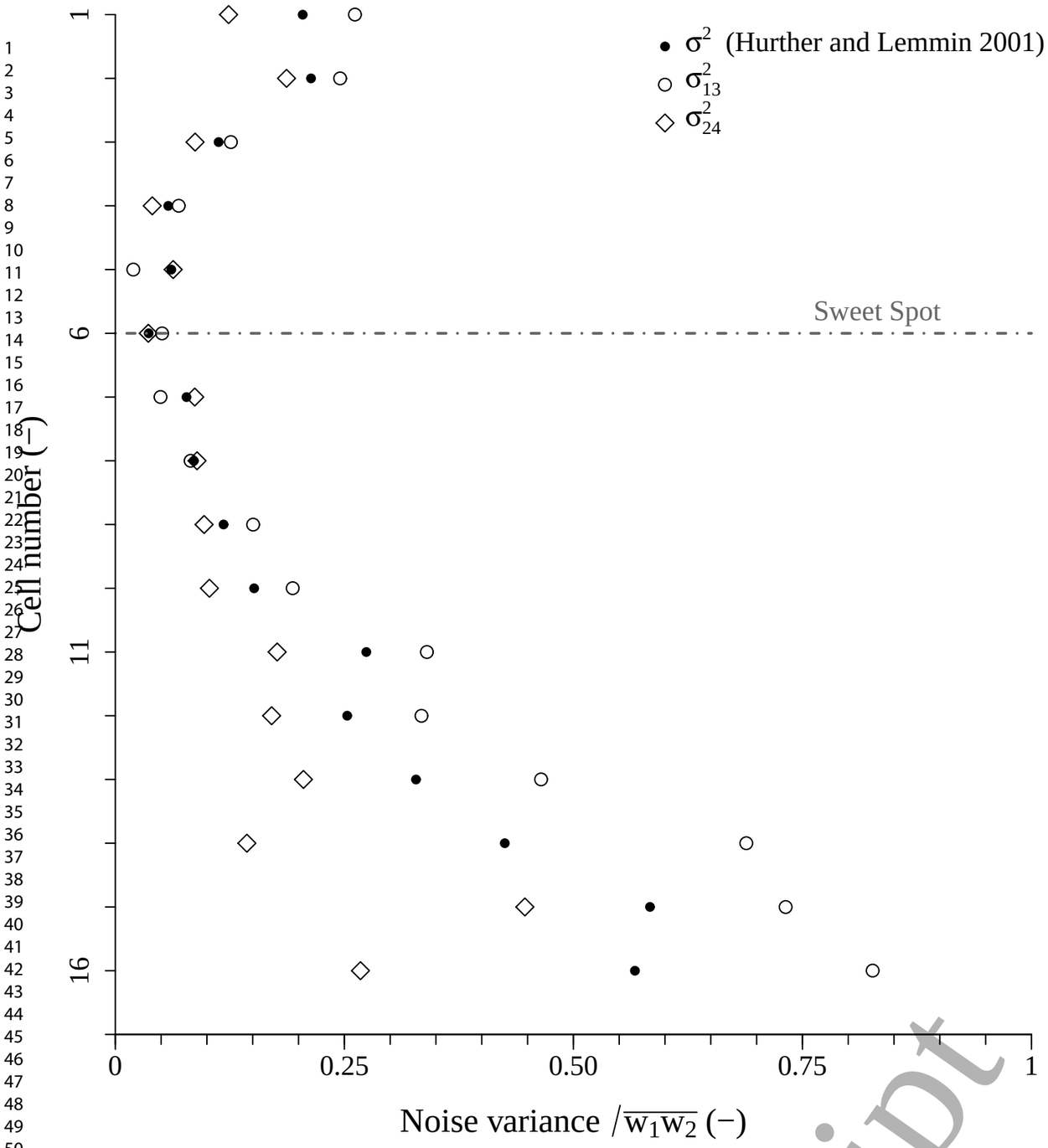

(b)

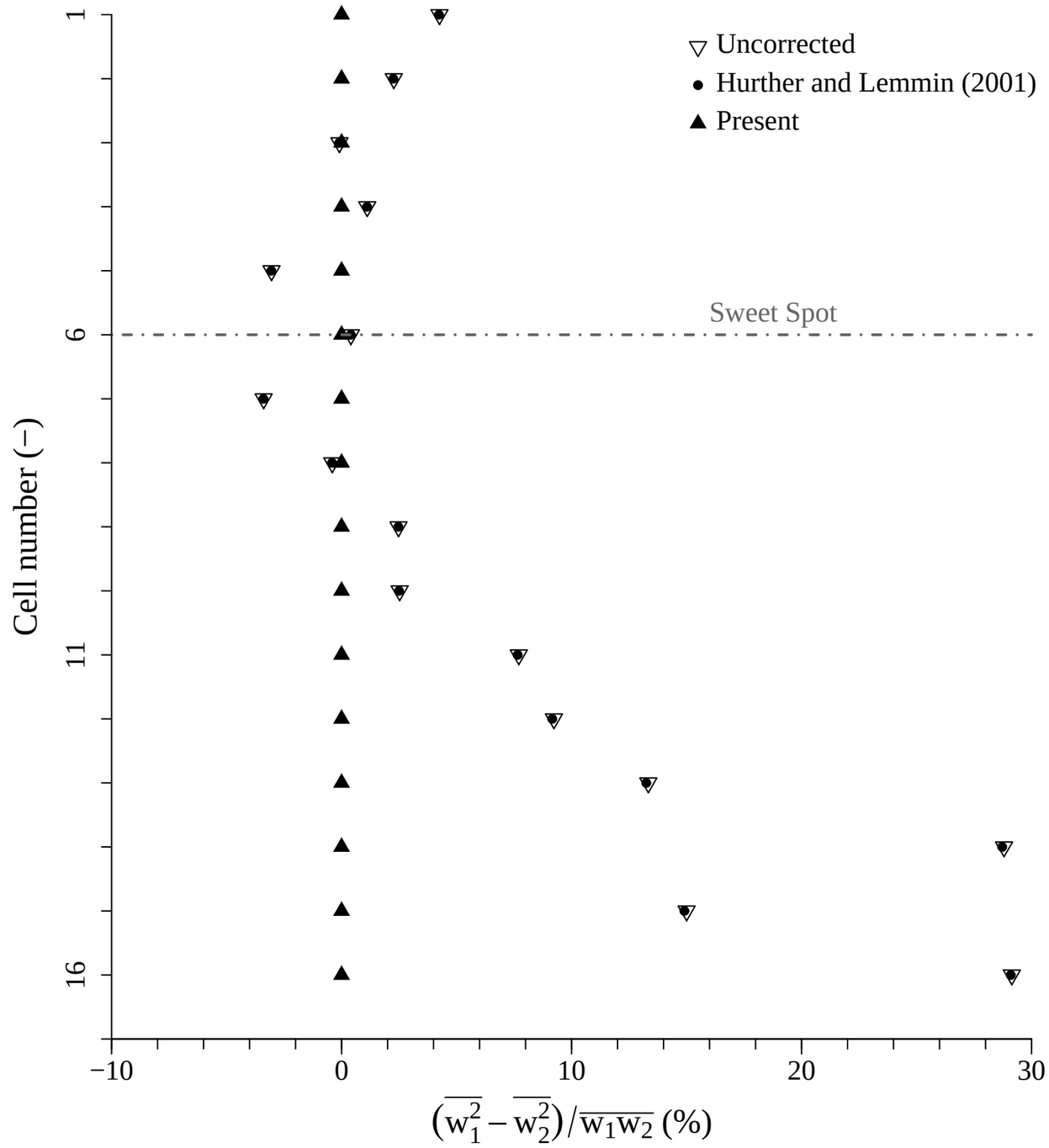

(c)

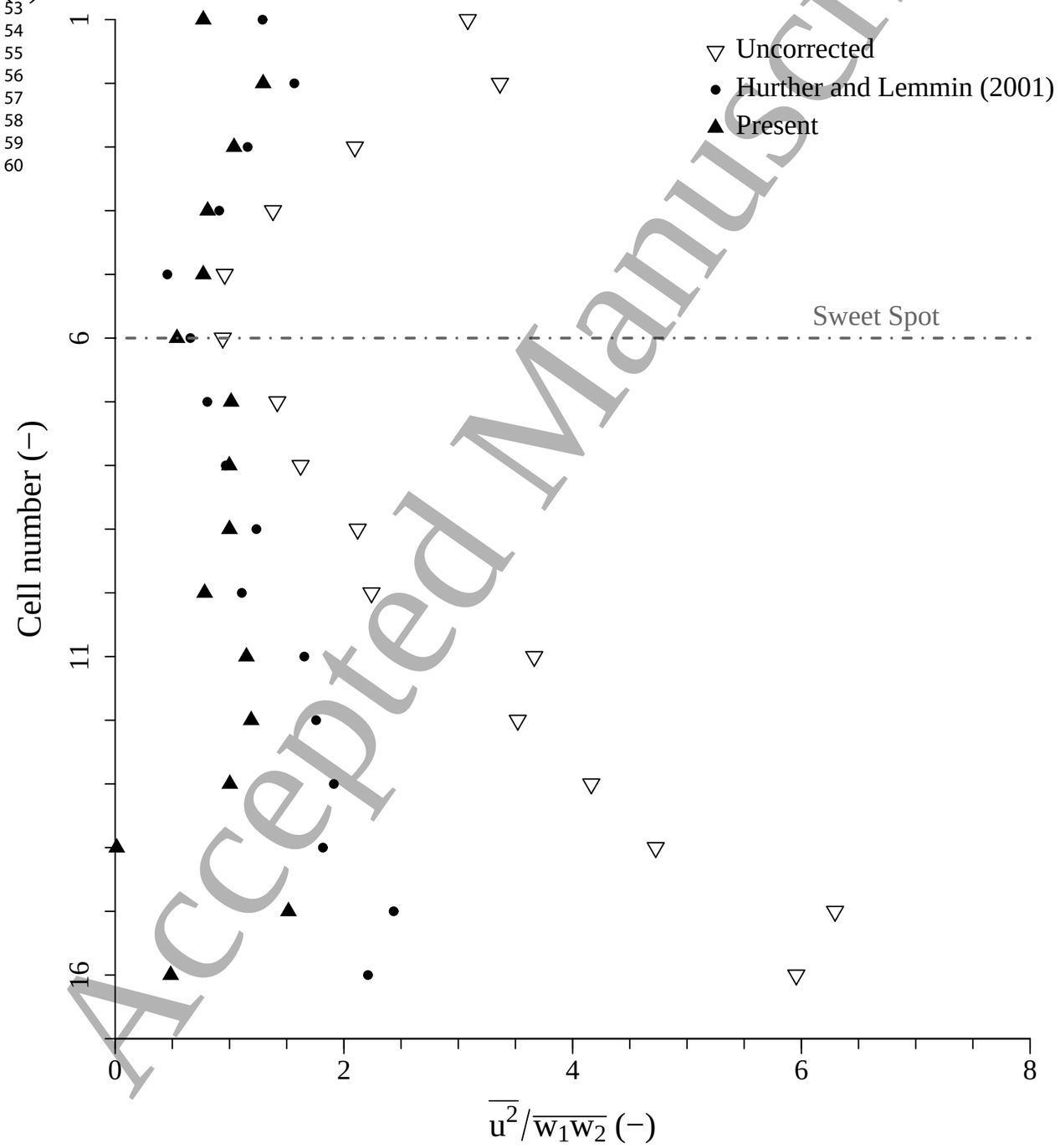

(d)